symmetry

MDPI

Article

Fault Diagnosis of High-Speed Rail Vehicle Suspension Systems: A Comparative Study of Koopman Operator and T–S Fuzzy Modeling Based Data-Driven K-Gap Metric

Zhoujie Lian [1], Yunkai Wu [1,*] and Yang Zhou [2]

[1] College of Automation, Jiangsu University of Science and Technology, Zhenjiang 212100, China; 241210301115@stu.just.edu.cn
[2] School of Computer Science and Engineering, Jiangsu University of Science and Technology, Zhenjiang 212100, China; jsjxy_zy@just.edu.cn
* Correspondence: wuyunkaischolar@just.edu.cn

Abstract

This paper proposes a novel data-driven K-Gap metric method based on the Koopman operator for the detection and isolation of multiplicative faults in high-speed train suspension systems. A systematic comparison is conducted with a data-driven K-Gap approach implemented through the fuzzy modeling framework. First, Takagi–Sugeno (T–S) theory is employed to extend the K-Gap metric for nonlinear dynamic modeling of the suspension system. Subsequently, the Koopman operator framework is introduced to lift the system states into a high-dimensional observable space, enabling a globally linear representation of the system. Building upon Koopman-based stable kernel representation (SKR), a more accurate K-Gap residual metric is constructed. Finally, a unified fault diagnosis scheme is developed with the K-Gap metric as the core indicator, and the two approaches are experimentally compared in terms of their performance in detecting and isolating multiplicative faults. The experimental results demonstrate that the Koopman-based method significantly outperforms the T–S fuzzy model in terms of residual separability, fault classification accuracy, and diagnostic stability, confirming its effectiveness and superiority for fault diagnosis in complex nonlinear systems.

Keywords: Koopman operator; data-driven; fault diagnosis; k-gap metric; high-speed train suspension system

Check for updates

Academic Editor: Simone Fiori

Received: 21 May 2026
Revised: 25 June 2026
Accepted: 27 June 2026
Published: 30 June 2026

Copyright: © 2026 by the authors. Licensee MDPI, Basel, Switzerland. This article is an open access article distributed under the terms and conditions of the Creative Commons Attribution (CC BY) license.

1. Introduction

The high-speed train suspension system, a critical subsystem responsible for ensuring operational safety and ride comfort, directly influences the dynamic performance and operational reliability of rail vehicles [1–3]. With increasing complexity of operating environments, faults in suspension dampers, springs, and actuators have progressively emerged as potential sources of system performance degradation and even major accidents. Such faults typically manifest as gradual parameter drifts (e.g., damping coefficient attenuation, nonlinear stiffness variations), and are characterized by strong concealment, high dynamic coupling, and susceptibility to environmental noise interference. If not detected and isolated promptly, faults can accumulate progressively and evolve into catastrophic failures, posing serious threats to the safe operation of high-speed trains. Consequently, the development of highly sensitive and robust fault diagnosis methods has become a critical challenge that demands urgent solutions in the field of rail transportation.

Current research on the diagnosis of faults in high-speed train suspension systems focuses primarily on two categories of approaches: model-based [4–7] and data-driven [8–11]. Model-based fault diagnosis methods operate by constructing precise physical or mathematical models and employing techniques such as residual generation, parameter estimation, or observer design. However, during operation, high-speed train suspension systems are frequently subject to strong nonlinearities (e.g., aging characteristics of rubber components), time-varying loads (e.g., track irregularity excitation), and multi-source uncertainties (e.g., sensor noise and unmodeled dynamics). These factors lead to significant model mismatch issues, making conventional residual analysis methods susceptible to interference and ineffective in distinguishing subtle faults from system uncertainties. In contrast, data-driven methods utilize historical or real-time operational data to achieve fault identification under model-free or weakly modeled conditions. By employing techniques such as feature extraction, statistical learning, and subspace analysis, these approaches offer advantages including reduced dependency on accurate modeling and enhanced adaptability. In the context of fault detection, commonly used data-driven techniques include Principal Component Analysis (PCA), Independent Component Analysis (ICA), and deep learning. In recent years, with improved data acquisition capabilities in rail transit systems and advances in data mining technologies, data-driven fault diagnosis has become a prominent research focus.

Although existing research has made progress in detecting and identifying faults in high-speed train suspension systems [12,13], diagnostic research specifically targeting faults caused by minute variations in structural parameters remains limited. Such faults multiplicatively affect the dynamic structure of the system, inducing no significant observable changes in the output during their initial stages. Moreover, they are often intrinsic to the system model, making them difficult to distinguish from environmental disturbances and measurement noise. In addition, high-speed train suspension systems typically operate under closed-loop control. The control loop actively suppresses the influence of fault-induced disturbances on system output, further obscuring the characteristic signatures of multiplicative faults and amplifying the complexity and technical challenges associated with their detection. Given that multiplicative faults can be induced by perturbations in system parameters, potentially compromise closed-loop characteristics or even induce instability [14,15], a method capable of directly assessing the impact of such faults on closed-loop system performance is essential. The gap metric, which precisely quantifies the impact of system variations induced by multiplicative faults, serves as a powerful diagnostic tool for such faults [16]. Originating from robust control theory, the gap metric was first proposed by Zames and El-Sakkary in 1980. It quantifies the "dynamic distance" between two systems within a closed-loop control structure, specifically measuring the distinguishability of their behaviors under identical feedback conditions. Particularly in data-driven scenarios, the gap metric can be applied without requiring complete system models or with only partial model knowledge by utilizing techniques such as subspace methods, system identification, or kernel-based approaches. This strategy substantially improves the detection sensitivity and robustness. Refs. [17,18] established coprime factorization and gap metric techniques for designing model-based and performance-based fault detection and isolation (FDI) frameworks. These works introduced the K-gap metric as an indicator for fault detectability analysis, and proposed definitions for fault detectability indices and fault-to-uncertainty ratios to handle FDI systems subject to multiplicative faults. Building on this foundation, ref. [19] advanced the K-gap metric technique by developing a data-driven scheme for its implementation. This scheme was utilized as both a detectability index and an isolability index for fault detection and isolation tasks. Subsequently, ref. [20] conducted a more in-depth investigation into data-driven computational methods for the

gap metric and its associated stability margin. Ref. [21] devised a hybrid fault diagnosis scheme that integrates model-based and data-driven gap metrics. Complementing this work, ref. [22] proposed a fault classification and grading framework specifically for subtle faults, and developed a data-driven gap metric-based FDI method within this framework.

Data-driven fault detection methods based on the gap metric have been extensively applied to linear time-invariant (LTI) multi-input multi-output (MIMO) systems in the existing literature, demonstrating both strong theoretical performance and practical potential. However, the dynamic behavior of high-speed train suspension systems during actual operation exhibits a significant deviation from the LTI assumption [23], due to complex factors such as nonlinear damping, nonlinear elastic stiffness and frictional hysteresis. Persistent reliance on linear modeling approaches can result in insufficient modeling accuracy and compromised diagnostic performance, thereby failing to meet the requirements of practical engineering applications. Consequently, it is necessary to extend gap metric-based methods from traditional linear systems to nonlinear systems to address the fault detection requirements of suspension systems under real-world operating conditions. Various methods are currently available for the analysis and modeling of nonlinear systems. A widely adopted technique is the Takagi—Sugeno (T–S) fuzzy model. As described in [24,25], this approach partitions a nonlinear system into multiple local linear subsystems and synthesizes them via fuzzy weighting. This methodology effectively captures nonlinear characteristics while retaining the advantage of analysis using linear tools. In contrast to piecewise-linear approximation methods such as the T–S fuzzy model, the Koopman operator framework does not rely on local approximations of nonlinear systems. Instead, it lifts the original state space into a new observable space, where the nonlinear dynamics can be characterized by a globally linear operator. This mechanism preserves the intrinsic features of the nonlinear dynamics while enabling the application of linear system analysis tools. In practical implementations, finite-dimensional approximations of the Koopman operator, such as extended dynamic mode decomposition (EDMD), are commonly employed to derive a linear representation of nonlinear systems directly from data. From a structural perspective, the Koopman-based modeling approach transforms a nonlinear system into a linear (or approximately linear) representation in a high-dimensional space. Consequently, the Koopman framework provides a feasible pathway for extending gap metric-based fault diagnosis methods from linear systems to nonlinear systems.

Recent years have witnessed significant breakthroughs in the control of nonlinear systems based on Koopman operator theory [26–28]. For example, ref. [29] utilizes this theory to construct an explicit dynamic model for soft robots through a data-driven approach, achieving precise manipulation through the application of mature model-based control methods. As demonstrated in [30], an interpretable Koopman operator-based deep neural network modeling method is proposed for data-driven modeling. When integrated with model predictive control (MPC), this approach achieves high-precision modeling and efficient motion control for autonomous vehicle dynamics.

In recent years, Koopman operator theory has also found increasing applications in nonlinear FDI. In ref. [31], a data-driven actuator fault detection method was proposed. By learning invariant basis functions through deep neural networks, Koopman-based linear predictors are constructed, thereby enabling global fault detection without relying on analytical models. In ref. [32], Koopman-based lifted linear models were integrated with Luenberger observers to generate residuals for actuator fault identification in nonlinear systems, allowing conventional linear FDI techniques to be applied to complex nonlinear dynamics. The aforementioned studies have demonstrated the effectiveness of integrating Koopman operators with observer design for signal-level residual generation. However, the structural discrepancies between nominal and faulty systems, particularly in the context

of multiplicative actuator faults, have yet to be quantitatively characterized from a system-theoretic perspective.

Building on the aforementioned background and to address the technical challenges of detecting and isolating multiplicative faults within the closed-loop architecture, this study leverages the complementary advantages of Koopman operator theory and the gap metric. The aim is to realize data-driven fault diagnosis for nonlinear closed-loop systems, such as high-speed train suspensions. The former accurately captures the dynamic evolution of the nonlinear system in a high-dimensional linearized space, while the latter quantifies structural discrepancies between systems. This integrated approach effectively preserves the dynamic characteristics of the system, enhances the distinguishability of fault features, and ensures the accuracy of the modeling. The main contributions of this work are as follows:

(1) We propose a data-driven online stable kernel representation (SKR) calculation method for nonlinear suspension systems of high-speed trains, grounded in Koopman operator theory. By leveraging the operator's ability to provide a global linear mapping of nonlinear dynamics, this method enables online estimation of the SKR without relying on an explicit system model.

(2) We utilized the global linearization capability of the Koopman operator to extend the data-driven K-Gap metric to nonlinear systems. This effectively overcomes the limitation of traditional methods that depend on LTI assumptions, enabling the detection of multiplicative faults.

(3) The proposed fault isolation method constructs a global linear embedding strategy via the Koopman operator, which provides a globally linear description of the nonlinear suspension system in a high-dimensional observable space. This approach addresses the limitations of traditional T–S fuzzy models in fault diagnosis, such as the reliance on local linearization and sensitivity to rule base configuration. Consequently, it effectively mitigates the loss of feature information caused by ambiguous fault characteristics and alleviates fault isolation difficulties stemming from overlapping fault clusters among multiple types of faults.

2. Preliminaries and Problem Formulation

2.1. SKR-Based System Description and Model-Based K-Gap Metric

Consider a discrete-time MIMO system $G(z)$ operating in an open-loop configuration as

$$y(z) = G(z)u(z), \tag{1}$$

where $u \in \mathbb{R}^l$ and $y \in \mathbb{R}^m$ denote the input and output vectors, respectively. An equivalent state-space realization of this system is given by

$$G : \begin{cases} x(k+1) = Ax(k) + Bu(k) + w(k), \\ y(k) = Cx(k) + v(k), \end{cases} \tag{2}$$

where $x(k) \in \mathbb{R}^n$ is the state vector, A, B and C are system matrices of compatible dimensions. The terms $w(k)$ and $v(k)$ represent zero-mean Gaussian processes and measurement noise, respectively.

In the absence of noise, i.e., when $w(k) = 0$ and $v(k) = 0$, the system admits a normalized left coprime factorization (LCF) of the form as

$$y(z) = G(z)u(z) = \hat{M}^{-1}(z)\hat{N}(z)u(z). \tag{3}$$

then the SKR is given by

$$\mathcal{K}(z)\begin{bmatrix} u(z) \\ y(z) \end{bmatrix} = \begin{bmatrix} -\hat{N}(z) & \hat{M}(z) \end{bmatrix}\begin{bmatrix} u(z) \\ y(z) \end{bmatrix} = 0 \tag{4}$$

where $\hat{M}(z)$ and $\hat{N}(z)$ constitute the LCF of $G(z)$.

Furthermore, the model-based K-Gap metric between two systems characterized by SKRs $\mathcal{K}_1$ and $\mathcal{K}_2$ is defined as

$$\delta_K(\mathcal{K}_1, \mathcal{K}_2) = \sup_{\substack{\begin{bmatrix} u_1 \\ y_1 \end{bmatrix} \in \mathcal{K}_1 \\ \begin{bmatrix} u_2 \\ y_2 \end{bmatrix} \in \mathcal{K}_2}} \inf \frac{\left\| \begin{bmatrix} u_1 \\ y_1 \end{bmatrix} - \begin{bmatrix} u_2 \\ y_2 \end{bmatrix} \right\|_2}{\left\| \begin{bmatrix} u_1 \\ y_1 \end{bmatrix} \right\|_2}, \tag{5}$$

where each subspace $\mathcal{K}_i \subset \mathcal{H}_2$ is defined as

$$\mathcal{K}_i = \left\{ \begin{bmatrix} u_i \\ y_i \end{bmatrix} \in \mathcal{H}_2 : \begin{bmatrix} -\hat{N}_i(z) & \hat{M}_i(z) \end{bmatrix}\begin{bmatrix} u_i \\ y_i \end{bmatrix} = 0 \right\}, i = 1, 2.$$

Alternatively, this metric admits an equivalent formulation as a model matching problem:

$$\delta_K(\mathcal{K}_1, \mathcal{K}_2) = \inf_{Q \in \mathcal{H}_\infty} \left\| \begin{bmatrix} -\hat{N}_1(z) & \hat{M}_1(z) \end{bmatrix} - Q(z) \begin{bmatrix} -\hat{N}_2(z) & \hat{M}_2(z) \end{bmatrix} \right\|_\infty$$

where $\delta_K(\mathcal{K}_1, \mathcal{K}_2) = \delta_K(\mathcal{K}_2, \mathcal{K}_1) \in (0, 1)$ holds due to the symmetric nature of the metric.

2.2. Data-Driven Realizations of SKR and Fault Indicator Design

To facilitate the data-driven design of fault detection and isolation schemes, we introduce the following input/output (I/O) representation of the system.

$$\mathbf{y}_s(k) = \Gamma_s x(k) + H_{u,s}\mathbf{u}_s(k) + H_{w,s}\mathbf{w}_s(k) + \mathbf{v}_s(k) \tag{6}$$

where $\mathbf{u}_s(k)$ and $\mathbf{y}_s(k)$ represent the input and output vectors as follows, with s denoting the length of the data set.

$$\mathbf{u}_s(k) = \begin{bmatrix} u(k-s+1) \\ \vdots \\ u(k) \end{bmatrix} \in \mathbb{R}^{s \times \ell}, \mathbf{y}_s(k) = \begin{bmatrix} y(k-s+1) \\ \vdots \\ y(k) \end{bmatrix} \in \mathbb{R}^{s \times m} \tag{7}$$

where $\Gamma_s \in \mathbb{R}^{sm \times n}$, $H_{u,s} \in \mathbb{R}^{sm \times s\ell}$, and $H_{w,s} \in \mathbb{R}^{sm \times sn}$.

Furthermore, stacked matrices $U_{k,s}$ and $Y_{k,s}$ can be defined as

$$U_{k,s} = \begin{bmatrix} u(k-s+1) & \cdots & u(k-s+N) \\ u(k-s+2) & \cdots & u(k-s+N+1) \\ \vdots & \ddots & \vdots \\ u(k) & \cdots & u(k+N-1) \end{bmatrix},$$
$$Y_{k,s} = \begin{bmatrix} y(k-s+1) & \cdots & y(k-s+N) \\ y(k-s+2) & \cdots & y(k-s+N+1) \\ \vdots & \ddots & \vdots \\ y(k) & \cdots & y(k+N-1) \end{bmatrix} \tag{8}$$

The above-mentioned matrices can be equivalently expressed as

$$U_{k,s} = \begin{bmatrix} \mathbf{u}_s(k) & \cdots & \mathbf{u}_s(k+N-1) \end{bmatrix}, Y_{k,s} = \begin{bmatrix} \mathbf{y}_s(k) & \cdots & \mathbf{y}_s(k+N-1) \end{bmatrix} \tag{9}$$

with $U_{k,s} \in \mathbb{R}^{s\ell \times N}$, $Y_{k,s} \in \mathbb{R}^{sm \times N}$ and N denoting the length of the data set.

Based on Equations (7) and (10), the I/O data model is given by

$$Y_{k,s} = \Gamma_s X_k + H_{u,s} U_{k,s} + H_{w,s} W_{k,s} + V_{k,s} \tag{10}$$

and it can be further expressed as

$$\begin{bmatrix} U_{k,s} \\ Y_{k,s} \end{bmatrix} = \begin{bmatrix} I & 0 \\ H_{u,s} & \Gamma_s \end{bmatrix} \begin{bmatrix} U_{k,s} \\ X_k \end{bmatrix} + \begin{bmatrix} 0 \\ H_{w,s} W_{k,s} + V_{k,s} \end{bmatrix} \tag{11}$$

Construct the following Hankel matrices:

$$Z_p = \begin{bmatrix} U_p \\ Y_p \end{bmatrix}, \quad Z_f = \begin{bmatrix} U_f \\ Y_f \end{bmatrix} \tag{12}$$

where $U_p = U_{k-s,s}$, $Y_p = Y_{k-s,s}$, $U_f = U_{k,s}$, $Y_f = Y_{k,s}$, with subscripts p and f denoting past and future, respectively.

The data-driven SKR $\mathcal{K}_{d,s}$ of system G can be characterized by the following condition:

$$\mathcal{K}_{d,s} \begin{bmatrix} U_f \\ Y_f \end{bmatrix} = \mathcal{K}_{d,s} \begin{bmatrix} U_{k,s} \\ Y_{k,s} \end{bmatrix} = 0 \tag{13}$$

s.t. $\mathcal{K}_{d,s} \begin{bmatrix} I & 0 \\ H_{u,s} & \Gamma_s \end{bmatrix} = 0$.

It can be computed by the LQ decomposition of input and output data as

$$\begin{bmatrix} Z_p \\ U_f \\ Y_f \end{bmatrix} = \begin{bmatrix} L_{11} & 0 & 0 \\ L_{21} & L_{22} & 0 \\ L_{31} & L_{32} & L_{33} \end{bmatrix} \begin{bmatrix} Q_1 \\ Q_2 \\ Q_3 \end{bmatrix} \tag{14}$$

Then one can obtain

$$\begin{bmatrix} U_f \\ Y_f \end{bmatrix} = \begin{bmatrix} L_{21} & L_{22} \\ L_{31} & L_{32} \end{bmatrix} \begin{bmatrix} Q_1 \\ Q_2 \end{bmatrix} + \begin{bmatrix} 0 \\ L_{33} Q_3 \end{bmatrix} \tag{15}$$

where $L_{33} Q_3 = H_{w,s} W_{k,s} + V_{k,s}$.

From Equations (9) and (13), the following relationship can be derived.

$$\Psi_s \begin{bmatrix} U_f \\ X_k \end{bmatrix} = \begin{bmatrix} L_{21} & L_{22} \\ L_{31} & L_{32} \end{bmatrix} \begin{bmatrix} Q_1 \\ Q_2 \end{bmatrix} \tag{16}$$

$$\Psi_s^{\perp}\Psi_s = 0 \Longleftrightarrow \Psi_s^{\perp} \begin{bmatrix} L_{21} & L_{22} \\ L_{31} & L_{32} \end{bmatrix} = 0 \tag{17}$$

Consequently, the data-driven SKR can be represented as follows:

$$\mathcal{K}_{d,s} = \begin{bmatrix} -\Gamma_s^{\perp} H_{u,s} & \Gamma_s^{\perp} \end{bmatrix} = \begin{bmatrix} L_{32}L_{22}^{\dagger}L_{21}L_{11}^{\dagger} - L_{31}L_{11}^{\dagger} & -L_{32}L_{22}^{\dagger} & I \end{bmatrix} \tag{18}$$

where $(\cdot)^{\dagger}$ denotes the pseudo-inverse.

Furthermore, the normalized data-driven SKR $\hat{\mathcal{K}}_{d,s}$ is given by

$$\bar{\mathcal{K}}_{d,s} = V_1^T \tag{19}$$

where V_1^T is obtained from the following singular value decomposition (SVD).

$$\mathcal{K}_{d,s} = U\Sigma V^T = U \begin{bmatrix} \Sigma_1 & 0 \end{bmatrix} \begin{bmatrix} V_1^T \\ V_2^T \end{bmatrix}$$

As established in [19], given the SKRs $\mathcal{K}^{(1)}$ and $\mathcal{K}^{(2)}$ derived from systems $G^{(1)}$ and $G^{(2)}$, the data-driven K-Gap can be computed as

$$\delta_{K_{d,s}}\left(\mathcal{K}^{(1)}, \mathcal{K}^{(2)}\right) = \bar{\sigma}\left(\left[I - (\bar{\mathcal{K}}_{d,s}^{(2)})^{\top}\bar{\mathcal{K}}_{d,s}^{(2)}\right]\left[(\bar{\mathcal{K}}_{d,s}^{(1)})^{\top}\bar{\mathcal{K}}_{d,s}^{(1)}\right]\right) \tag{20}$$

As the data length parameter $s \to \infty$, the data-driven K-Gap converges to its model-based counterpart:

$$\delta_{K_{d,s}}(\mathcal{K}^{(1)}, \mathcal{K}^{(2)}) \to \delta_K(\mathcal{K}^{(1)}, \mathcal{K}^{(2)})$$

Building upon the K-Gap metric, this paper can further propose a residual-induced minimum fitting distance measure. This measure quantifies the similarity between real-time residual data and a pre-constructed fault dictionary, thereby serving as a practical fault detection indicator.

3. T–S Fuzzy Modelling and FDD Indicator Design

3.1. T–S Fuzzy Modeling for Suspension Systems

We established differential equations for the suspension dynamics of high-speed trains in [24]. Building on this model, we construct the system dynamics by explicitly incorporating track irregularity and active control forces as critical inputs. These forces are represented by the vector $u(k) = [ff_r, ff_l, fr_r, fr_l, d]^{\top}$. The output is defined as $y(k) = [z_0, \phi_0, \theta_0, z_1, \phi_1, \theta_1, z_2, \phi_2, \theta_2]^{\top}$; The state vector is $x(k) = [z_0, \phi_0, \theta_0, z_1, \phi_1, \theta_1, z_2, \phi_2, \theta_2, \dot{z}0, \dot{\phi}0, \dot{\theta}0, \dot{z}1, \dot{\phi}1, \dot{\theta}1, \dot{z}2, \dot{\phi}2, \dot{\theta}2]^{\top}$. Here, we denote the vertical displacement, pitch, and roll angles in the c.g. of the carbody ($i = 0$), front bogie ($i = 1$), and rear bogie ($i = 2$) as z_i, ϕ_i, and θ_i. The inputs include active control forces ff_r, ff_l, fr_r, fr_l, and the vertical wheel-rail contact displacement d obtained from the track spectrum.

The state-space representation of this nonlinear suspension system is given by

$$G: \begin{cases} x(k+1) = g(x,k) + Bu(k) + w(k) \\ y(k) = h(x,k) + v(k) \end{cases} \tag{21}$$

where $g(\cdot)$ and $h(\cdot)$ are continuously differentiable nonlinear functions with appropriate dimensions; B represent the input matrices, respectively, derived from the differential equations; $w(k)$ and $v(k)$ denote Gaussian-distributed process and measurement noise sequences.

Since the K-Gap method is designed for LTI systems but the train suspension is nonlinear, we utilize T–S fuzzy theory to construct a locally linearized model. This facilitates the use of K-Gap in diagnosing multiplicative faults within the system. Taking into account system (22), the locally linearized fault-free model of the high-speed train suspension system is expressed as follows:

Rule $\mathfrak{P}^i$: If $\eta_1(k)$ is $N_{1,i}$, $\eta_2(k)$ is $N_{2,i}$, $\cdots$, and $\eta_q(k)$ is $N_{q,i}$, then

$$\begin{cases} x(k+1) = A_i x(k) + Bu(k) + w(k) \\ y(k) = \mathcal{C}_i x(k) + v(k) \end{cases}, \ i \in \{1, 2, \cdots, \varrho\} \tag{22}$$

where a set of measurable premise variables $\eta(k) = \left[\eta_1(k), \eta_2(k), \cdots, \eta_q(k)\right]$. The system is described by ϱ fuzzy inference rules, where the i-th rule $\mathfrak{P}^i$ employs the fuzzy sets $N_{j,i}$ $(j = 1, 2, \ldots, q)$.

Then, the global form

$$G : \begin{cases} x(k+1) = \sum\limits_{i=1}^{\varrho} \mu_i(\eta(k))(A_i x(k) + Bu(k) + w(k)) \\ y(k) = \sum\limits_{i=1}^{\varrho} \mu_i(\eta(k))(\mathcal{C}_i x(k) + v(k)) \end{cases} \tag{23}$$

where the fuzzy membership functions $\mu_i(\eta(k))$ satisfy both the normalization condition $\sum_{i=1}^{\varrho} \mu_i(\eta(k)) = 1$ and the inequality $0 \leq \mu_i(\eta(k)) \leq 1$.

Similarly, the local T–S fuzzy I/O data model for the fault-free system G is derived as follows:

Rule $\mathfrak{P}^i$: If $\eta_1(k)$ is $N_{1,i}$, $\eta_2(k)$ is $N_{2,i}$, $\cdots$, and $\eta_q(k)$ is $N_{q,i}$, then

$$Y_{k,s} = \Gamma_{i,s} X_k + H_{i,u,s} U_{k,s} + H_{i,w,s} W_{k,s} + V_{k,s} \tag{24}$$

with

$$\Gamma_{i,s} = \begin{bmatrix} \mathcal{C}_i \\ \mathcal{C}_i A_i \\ \vdots \\ \mathcal{C}_i A_i^s \end{bmatrix}, \quad H_{i,u,s} = \begin{bmatrix} 0 & 0 & \cdots & 0 \\ \mathcal{C}_i B & 0 & \ddots & \vdots \\ \vdots & \ddots & \ddots & 0 \\ \mathcal{C}_i A_i^{s-1} B & \cdots & \mathcal{C}_i B & 0 \end{bmatrix}, \quad H_{i,w,s} = \begin{bmatrix} 0 & 0 & \cdots & 0 \\ \mathcal{C}_i & \ddots & \ddots & \vdots \\ \vdots & \ddots & \ddots & 0 \\ \mathcal{C}_i A_i^{s-1} & \cdots & \mathcal{C}_i & 0 \end{bmatrix}$$

3.2. T–S Fuzzy Based Data-Driven K-Gap Metric Design

Following Equation (15), the SKR under the fuzzy rule-based local linearization model can be derived similarly. The fuzzy data-driven SKR is obtained as follows:

$$\begin{bmatrix} Z_p \\ U_f \\ Y_f \end{bmatrix} = \begin{bmatrix} L_{i,11} & 0 & 0 \\ L_{i,21} & L_{i,22} & 0 \\ L_{i,31} & L_{i,32} & L_{i,33} \end{bmatrix} \begin{bmatrix} Q_{i,1} \\ Q_{i,2} \\ Q_{i,3} \end{bmatrix} \tag{25}$$

The local T–S fuzzy based data-driven SKR $\mathcal{K}_{i,d,s}$ is given by

Rule $\mathfrak{P}^i$: If $\eta_1(k)$ is $N_{1,i}$, $\eta_2(k)$ is $N_{2,i}$, $\cdots$, and $\eta_q(k)$ is $N_{q,i}$, then

$$\mathcal{K}_{i,d,s}^{\text{T–S}} = \begin{bmatrix} L_{i,32} L_{i,22}^{\dagger} L_{i,21} L_{i,11}^{\dagger} - L_{i,31} L_{i,21}^{\dagger} & -L_{i,32} L_{i,22}^{\dagger} & I \end{bmatrix} \tag{26}$$

The normalized local T–S fuzzy data-driven SKR

$$\bar{\mathcal{K}}_{i,d,s}^{\text{T–S}} = V_{i,1}^T \tag{27}$$

where $V_{i,1}^T$ is obtained from the SVD as

$$\mathcal{K}_{i,d,s}^{\text{T–S}} = U_i \Sigma_i V_i^T = U_i \begin{bmatrix} \Sigma_{i,1} & 0 \end{bmatrix} \begin{bmatrix} V_{i,1}^T \\ V_{i,2}^T \end{bmatrix}$$

The local T–S fuzzy based data-driven K-Gap metric is redefined as
Rule $\mathfrak{P}^i$: If $\eta_1(k)$ is $N_{1,i}$, $\eta_2(k)$ is $N_{2,i}$, $\cdots$, and $\eta_q(k)$ is $N_{q,i}$, then

$$\delta_{K_{i,d,s}}^{T--S}\left(\mathcal{K}_i^{(1)}, \mathcal{K}^{(2)}\right) = \bar{\sigma}\left(\left[I - \left(\bar{\mathcal{K}}_{d,s}^{(2)}\right)^T \bar{\mathcal{K}}_{d,s}^{(2)}\right]\left[\left(\bar{\mathcal{K}}_{i,d,s}^{\text{T–S}(1)}\right)^T \bar{\mathcal{K}}_{i,d,s}^{\text{T–S}(1)}\right]\right) \tag{28}$$

where $\mathcal{K}_i^{(1)}$ and $\bar{\mathcal{K}}_{i,d,s}^{\text{T–S}(1)}$ denote the i-th fuzzy SKR and normalized data-driven SKR for system G_1, while $\mathcal{K}^{(2)}$ and $\bar{\mathcal{K}}_{d,s}^{(2)}$ represent the SKR and the data-driven SKR for system G_2.

Remark 1. *Given the relatively short duration of the stacking window s, we assume that the system G_2 behaves linearly within this interval. Consequently, the normalized data-driven SKR $\bar{\mathcal{K}}_{d,s}^{(2)}$ for G_2 can be calculated using Equations (8)–(20).*

The global fuzzy data-driven K-Gap metric $\delta_{K_{d,s}}^{T--S}$ is defined as

$$\delta_{K_{d,s}}^{T--S}\left(\mathcal{K}^{(1)}, \mathcal{K}^{(2)}\right) = \sum_{i=1}^{\varrho} \mu_i(\eta(k)) \delta_{K_{i,d,s}}\left(\mathcal{K}_i^{(1)}, \mathcal{K}^{(2)}\right) \tag{29}$$

where $\mathcal{K}^{(1)}$ represents the global SKR for system G_1. The calculation of $\delta_{K_{d,s}}^{T--S}$ is summarized in Algorithm 1.

Algorithm 1 Implementation of T–S fuzzy data-driven K-Gap metric $\delta_{K_{d,s}}^{T--S}$

Require: I/O data u^1, y^1 of system G_1; u^2, y^2 of system G_2

Ensure: $\delta_{K_{d,s}}^{T--S}(\mathcal{K}^{(1)}, \mathcal{K}^{(2)})$

1. Initialization step: Set the fuzzy rule configuration, the time period K, and the data-driven parameters s and N.

2. Compute normalized SKR $\bar{\mathcal{K}}_{i,d,s}^{\text{T–S}(1)}$ for G_1 under each fuzzy rule using Equations (25)–(28).

3. For $k = 1$ to K

   3.1. Compute normalized SKR $\bar{\mathcal{K}}_{d,s}^{(2)}(k)$ for G_2 using Equations (8)–(20).

   3.2. Calculate local T–S fuzzy K-Gap metric $\delta_{K_{d,s}}^{T--S}(\mathcal{K}_i^{(1)}, \mathcal{K}^{(2)}(k))$ using Equation (29).

   3.3. Calculate global T–S fuzzy K-Gap metric $\delta_{K_{d,s}}^{T--S}(\mathcal{K}^{(1)}, \mathcal{K}^{(2)}(k))$ using Equation (30).

4. Return: $\delta_{K_{d,s}}^{T--S}(\mathcal{K}^{(1)}, \mathcal{K}^{(2)})$.

4. Koopman Modelling and FDD Indicator Design

4.1. Koopman Modelling for Suspension Systems

The Koopman operator typically captures the intrinsic dynamics of nonlinear systems through linear evolution. With appropriate modifications, its applicability can be extended to controlled dynamical systems. As an illustrative example, based on the previously established differential equation model, a discretized high-speed train suspension system, assuming no model uncertainty, can also be expressed in the following form:

$$\begin{cases} x(k+1) = g(x,k) + Bu(k) = f\big(x(k), u(k)\big) \\ y(k) = h(x,k) = Cx(k) \end{cases} \tag{30}$$

where k denotes the discrete-time index. C represents the input matrix, which can be derived from the differential equation model [24]. The construction of the Koopman operator is fundamentally dependent on the definition of the extended state vector $\chi = [x^{\mathsf{T}}, u^{\mathsf{T}}]^{\mathsf{T}} \in \mathbb{R}^n \times \ell'(\mathcal{U})$, where $u = (u_i)_{i=0}^{\infty}$ denotes the sequence of future control inputs and $\ell'(\mathcal{U})$ refers to the sequence space with each $u_i \in \mathcal{U}$. Under the assumption of linear control signal evolution, the system can be transformed from a time-varying (non-autonomous) framework into an equivalent state-driven, autonomous representation.

$$\chi(k+1) = F\big(\chi(k)\big) = \begin{bmatrix} f\big(x, \boldsymbol{u}(0)\big) \\ S\boldsymbol{u} \end{bmatrix} \tag{31}$$

where S denotes the shift operator, defined by $(S\boldsymbol{u})(i) = \boldsymbol{u}(i+1)$. Here, $\boldsymbol{u}(0) \in \mathbb{R}^m$ represents the current control input and corresponds to the initial element of the sequence $\boldsymbol{u}$.

Consequently, the Koopman operator for system (31), which is defined on the extended state χ, can be expressed as

$$(\mathcal{K}\phi)(\chi) = \phi\big(F(\chi)\big) \tag{32}$$

where $\mathcal{K}$ represents a Koopman operator in an infinite-dimensional functional space, and $\phi \in \mathbb{R}$ is an observable function defined in the lifted state space.

In practical applications, the focus is on constructing finite-dimensional approximations of the Koopman operator, $\mathcal{K}$. To this end, we extend the extended dynamic mode decomposition (EDMD) framework to accommodate systems with control inputs. The EDMD algorithm approximates the Koopman operator from the observed data by employing a set of predefined lifting functions as

$$\phi(\chi) = \begin{bmatrix} \phi_1(\chi) & \cdots & \phi_{N_\phi}(\chi) \end{bmatrix}^{\mathsf{T}} \tag{33}$$

where basis function $\phi_i : \mathbb{R}^n \times \ell'(\mathcal{U}) \to \mathbb{R}, i \in \{1, \ldots, N_\phi\}$ maps the extended state space to scalar observables. The finite-dimensional approximation $\mathcal{A}$ is determined by solving the following leasT–Squares optimization problem:

$$\min_{\mathcal{A}} \sum_{j=1}^{K} \left\| \phi(\chi_j^+) - \mathcal{A}\phi(\chi_j) \right\|_2^2 \tag{34}$$

To preserve linear prediction capability and computational tractability, lifting functions are assumed to be of the form of

$$\phi_i(x, \boldsymbol{u}) = \psi_i(x) + \mathcal{L}_i(\boldsymbol{u}) \tag{35}$$

where $\psi_i : \mathbb{R}^n \to \mathbb{R}$ is typically a nonlinear function, and $\mathcal{L}_i : \ell'(\mathcal{U}) \to \mathbb{R}$ is a linear operator on the control input sequence. Without loss of generality, one can set the number of lifting functions to $N_\phi = N + m$ for some $N > 0$. This allows the overall lifting process to be reformulated as

$$\phi(x, \boldsymbol{u}) = \begin{bmatrix} \psi(x) \\ \boldsymbol{u}(0) \end{bmatrix} \tag{36}$$

where $\psi(x) = [\psi_1(x), \ldots, \psi_N(x)]^\top$ encapsulates the nonlinear components dependent on the state, and $\boldsymbol{u}(0)$ denotes the current control input. Accordingly, the objective function can be rewritten in terms of lifted state features as

$$\min_{A_k, B_k} \sum_{j=1}^{K} \left\| \psi(x_j^+) - A_k \psi(x_j) - B_k \boldsymbol{u}_j(0) \right\|_2^2 \tag{37}$$

where the first N rows of the Koopman approximation matrix $\mathcal{A}$ are partitioned as $[A_k \mid B_k]$, with $A_k \in \mathbb{R}^{N \times N}$ and $B_k \in \mathbb{R}^{N \times m}$.

The decoder matrix C', which projects the lifted states back onto the original state space, is obtained by solving the following leasT–Squares problem.

$$\min_{C'} \sum_{j=1}^{K} \| x_j - C' \psi(x_j) \|_2^2 \tag{38}$$

Consider a dataset collected from the high-speed train suspension system, structured as follows:

$$\mathbf{X} = [x_1, \ldots, x_j], \mathbf{X}^+ = [x_2, \ldots, x_{j+1}], \mathbf{U} = [u_1, \ldots, u_j] \tag{39}$$

where j denotes the total number of samples.

The lifting process maps the collection of state snapshots into a higher-dimensional feature space as follows:

$$\mathbf{X}_{\text{lift}} = [\psi(x_1), \ldots, \psi(x_j)],\ \mathbf{X}_{\text{lift}}^+ = [\psi(x_2), \ldots, \psi(x_{j+1})] \tag{40}$$

Here, the lifting function is defined as $\psi(x) := \begin{bmatrix} \psi_1(x) \\ \vdots \\ \psi_N(x) \end{bmatrix}$, where $\{\psi_i\}_{i=1}^N$ denotes a set of predefined basis functions, such as monomials, trigonometric functions, or exponentials.

The matrices $A_k \in \mathbb{R}^{N \times N}$, $B_k \in \mathbb{R}^{N \times m}$, and $C' \in \mathbb{R}^{n \times N}$ are estimated by solving the following leasT–Squares optimization problems:

$$\begin{aligned} &\min_{A_k, B_k} \ \left\| \mathbf{X}_{\text{lift}}^+ - A_k \mathbf{X}_{\text{lift}} - B_k \mathbf{U} \right\|_F \\ &\min_{C'} \ \left\| \mathbf{X} - C' \mathbf{X}_{\text{lift}} \right\|_F \end{aligned} \tag{41}$$

where $\| \cdot \|_F$ denotes the Frobenius norm.

The closed-form solutions to the aforementioned problems are given by

$$[A_k, B_k] = \mathbf{X}_{\text{lift}}^+ [\mathbf{X}_{\text{lift}}, \mathbf{U}]^\dagger, \quad C' = \mathbf{X} \mathbf{X}_{\text{lift}}^\dagger \tag{42}$$

where $(\cdot)^\dagger$ denotes the Moore–Penrose pseudoinverse.

Finally, the Koopman linearized model for the nominal high-speed train suspension system is

$$\begin{cases} z(k+1) = A_k z(k) + B_k u(k) \\ y(k) \approx CC' z(k) = C_k z(k) \end{cases} \tag{43}$$

with initial condition $z_0 = \psi(x_0) = [\psi_1(x_0), \ldots, \psi_N(x_0)]^\top$, $CC' = C_k$.

Similarly, consider the multiplicative fault model of a high-speed train suspension system in the absence of model uncertainty as

$$\begin{cases} x^f(k+1) = g^f(x^f, k) + Bu^f(k) = f^f(x^f(k), u^f(k)) \\ y^f(k) = h(x^f, k) = Cx^f(k) \end{cases} \tag{44}$$

The corresponding Koopman linearized model is

$$\begin{cases} z^f(k+1) = A_k^f z^f(k) + B_k^f u^f(k) \\ y^f(k) \approx C_k^f z^f(k) \end{cases} \tag{45}$$

When model uncertainty is considered, the Koopman representations of both fault-free and faulty systems take the following form:

$$\mathrm{G}: \begin{cases} z(k+1) = A_k z(k) + B_k u(k) + w(k) \\ y(k) = C_k z(k) + v(k) \end{cases} \tag{46}$$

$$\mathrm{G}_f: \begin{cases} z^f(k+1) = A_k^f z^f(k) + B_k^f u^f(k) + w(k) \\ y^f(k) = C_k^f z^f(k) + v(k) \end{cases} \tag{47}$$

where $w(k)$ and $v(k)$ represent process and measurement noise, respectively.

Consider the Koopman model for a fault-free system,

$$Y_{k,s} = \Gamma_s^k Z_{k,s} + H_{u,s}^k U_{k,s} + H_{w,s}^k W_{k,s} + V_{k,s} \tag{48}$$

where $Z_{k,s}$, $U_{k,s}$ and $Y_{k,s}$ are Hankel matrices constructed from the state z, input u and output y, respectively. The system matrices

$$\Gamma_s^k = \begin{bmatrix} C_k \\ C_k A_k \\ \vdots \\ C_k A_k^s \end{bmatrix}, \quad H_{u,s}^k = \begin{bmatrix} 0 & 0 & \cdots & 0 \\ C_k B_k & \ddots & \ddots & \vdots \\ \vdots & \ddots & \ddots & 0 \\ C_k A_k^{s-1} B_k & \cdots & C_k B_k & 0 \end{bmatrix}, \quad H_{w,s}^k = \begin{bmatrix} 0 & 0 & \cdots & 0 \\ C_k & \ddots & \ddots & \vdots \\ \vdots & \ddots & \ddots & 0 \\ C_k A_k^{s-1} & \cdots & C_k & 0 \end{bmatrix} \tag{49}$$

4.2. Data-Driven K-Gap Metric in Koopman Model

As indicated by Equations (15)–(19), given that the system parameters of the Koopman model are known, the Koopman-based data-driven SKR $\mathcal{K}_{d,s}^k$ can also be calculated using the following expression:

$$\mathcal{K}_{d,s}^k = \begin{bmatrix} -\Gamma_s^{\perp} H_{u,s}^k & \Gamma_s^{\perp +} \end{bmatrix} \tag{50}$$

Then, perform an SVD to obtain the normalized Koopman-based data-driven SKR, denoted as $\bar{\mathcal{K}}_{d,s}^{k}$. Finally, the Koopman-based data-driven K-Gap metric $\delta_{K_{d,s}}^{k}$ can be expressed as follows:

$$\begin{aligned} &\delta_{K_{d,s}}^{k}\left(\mathcal{K}_{K}^{(1)}, \mathcal{K}_{K}^{(2)}\right) \\ &= \bar{\sigma}\left(\left[I - \left(\bar{\mathcal{K}}_{d,s}^{k(2)}\right)^{\mathsf{T}} \bar{\mathcal{K}}_{d,s}^{k(2)}\right]\left(\bar{\mathcal{K}}_{d,s}^{k(1)}\right)^{\mathsf{T}} \bar{\mathcal{K}}_{d,s}^{k(1)}\right) \end{aligned} \tag{51}$$

where $\bar{\mathcal{K}}_{d,s}^{k(1)}$ and $\bar{\mathcal{K}}_{d,s}^{k(2)}$ respectively represent the normalized Koopman-based data-driven SKR of system G_1 and G_2. The calculation of $\delta_{K_{d,s}}^{k}$ is summarized in Algorithm 2.

Algorithm 2 Implementation of Koopman-Based Data-Driven K-Gap Metric $\delta_{K_{d,s}}^{k}$

1. Input-output data u^1, x^1 of system G_1; u^2, x^2 of system G_2;
2. Initialize the time period K, data-driven parameter s, and recorded data points j_i;
3. Construct the datasets $\mathbf{X}_1^{+}$, $\mathbf{X}_1$, $\mathbf{U}_1$ for system G_1 according to Equation (40);
4. Compute A_1^k, B_1^k, C_1^k for system G_1 offline using Equation (43);
5. Obtain the Koopman-based SKR $\overline{\mathcal{K}}_{d,s}^{k(1)}$ according to Equation (50), and normalize it using Equation (20);
6. **For** $k = 1$ **to** K;
   6.1 Construct the datasets $\mathbf{X}_2^{+}$, $\mathbf{X}_2$, $\mathbf{U}_2$ for system G_2;
   6.2 Compute A_2^k, B_2^k, C_2^k for system G_2 online;
   6.3 Obtain the normalized SKR $\overline{\mathcal{K}}_{d,s}^{k(2)}$ for the current instant k;
   6.4 Calculate $\delta_{K_{d,s}}^{k}\left(\mathcal{K}_{K}^{(1)}, \mathcal{K}_{K}^{(2)}\right)$ using Equation (51);
7. **End For**;
8. **Return** $\delta_{K_{d,s}}^{k}\left(\mathcal{K}_{K}^{(1)}, \mathcal{K}_{K}^{(2)}\right)$.

5. The Fault Detection and Isolation Scheme

5.1. The Fault Detection Scheme

In the preceding sections, we have presented data-driven evaluations of the K-Gap metric for nonlinear systems using two approaches: T–S fuzzy local linearization and global linearization based on the Koopman operator. Based on these methodologies, the following conclusions can be drawn:

$$J(k) = \begin{cases} \delta_{K_{d,s}}^{T--S}\left(\mathcal{K}^{(o)}, \mathcal{K}^{(f)}(k)\right) & \text{T–S fuzzy model} \\ \delta_{K_{d,s}}^{k}\left(\mathcal{K}_{K}^{(o)}, \mathcal{K}_{K}^{(f)}(k)\right) & \text{Koopman model} \end{cases} \tag{52}$$

where $\mathcal{K}^{(o)}$ and $\mathcal{K}_{K}^{(o)}$ are SKRs of the fault-free system, $\mathcal{K}^{(f)}(k)$ and $\mathcal{K}_{K}^{(f)}(k)$ are SKRs of the faulty system. For each instant of time k in the faulty system, one can obtain its corresponding SKR, $\mathcal{K}^{(f)}(k)$ or $\mathcal{K}_{K}^{(f)}(k)$, via data-driven modeling and conduct a comparison of the K-Gap metric with the fault-free system.

Consequently, a straightforward and effective fault detection scheme can be implemented on the basis of the K-Gap metric. The detection logic is as follows:

$$\begin{cases} J \leq J_{th} & \text{fault-free} \\ J > J_{th} & \text{faulty} \end{cases} \tag{53}$$

where J_{th} is the threshold derived from historical data for the fault-free system.

5.2. The Fault Isolation Scheme

Furthermore, the K-Gap metric offers a powerful tool for fault isolation by quantifying the extent to which different faults alter the system dynamic structure. Since an equivalent linear Koopman model of the high-speed train suspension system has been established in the preceding analysis, we now consider two Koopman-based representations, denoted as $G_K^{(f_1)}$ and $G_K^{(f_2)}$, corresponding to two distinct fault modes for subsequent fault diagnosis studies. Each representation yields a distinct model-based SKR, denoted as $\mathcal{K}_K^{(f_1)}$ and $\mathcal{K}_K^{(f_2)}$ respectively. The K-Gap metric between them is then defined as

$$\delta_k\left(\mathcal{K}_K^{(f_1)}, \mathcal{K}_K^{(f_2)}\right) = \inf_{Q \in H_\infty} \left\| \left[-\hat{N}_{f_1}^k \hat{M}_{f_1}^k\right] - Q\left[-\hat{N}_{f_2}^k \hat{M}_{f_2}^k\right] \right\|_\infty \tag{54}$$

where $G_K^{(f_1)} = \hat{M}_{f_1}^k \hat{N}_{f_1}^k$ and $G_K^{(f_2)} = \hat{M}_{f_2}^k \hat{N}_{f_2}^k$ are the left coprime factorization of the system.

Based on Equation (4), consider introducing a postfilter $R(z)$ to enhance the discrimination between different Koopman-based faulty models. Let

$$\| \mathrm{R}\left[-\hat{N}_{f_1}^k \ \hat{M}_{f_1}^k\right] \begin{bmatrix} u_{f_1} \\ y_{f_1} \end{bmatrix} \|_2 \gg \| \mathrm{R}\left[-\hat{N}_{f_2}^k \ \hat{M}_{f_2}^k\right] \begin{bmatrix} u_{f_2} \\ u_{f_2} \end{bmatrix} \|_2 \tag{55}$$

where $\begin{bmatrix} u_{f_1} \\ y_{f_1} \end{bmatrix}, \begin{bmatrix} u_{f_2} \\ y_{f_2} \end{bmatrix} \in \mathcal{H}_2, \|\mathrm{R}\|_\infty = 1$.

As noted in [33], Equation (54) can be equivalently formulated as

$$\delta_k\left(\mathcal{K}_K^{(f_1)}, \mathcal{K}_K^{(f_2)}\right) = \inf_{Q \in H_\infty} \sup_{\|\xi\|_2 = 1} \|(\hat{H}_{f_1}^k - Q\hat{H}_{f_2}^k)\xi\|_2 = \sup_{\|\xi\|_2 = 1} \inf_{\eta \in H_2} \|\hat{H}_{f_1}^k \xi - \hat{H}_{f_2}^k \eta\|_2 \tag{56}$$

where $\hat{H}_{f_1}^k = [-\hat{N}_{f_1}^k \ \hat{M}_{f_1}^k]$, $\hat{H}_{f_2}^k = [-\hat{N}_{f_2}^k \ \hat{M}_{f_2}^k]$ and $\xi = \begin{bmatrix} u_{f_1} \\ y_{f_1} \end{bmatrix}, \eta = \begin{bmatrix} u_{f_2} \\ y_{f_2} \end{bmatrix}$.

According to Equation (56), let the graph operators of the two systems be denoted by $\hat{H}_{f_1}^k$ and $\hat{H}_{f_2}^k$. The K-gap can be written as

$$\delta_k\left(\mathcal{K}_K^{(f_1)}, \mathcal{K}_K^{(f_2)}\right) = \sup_{\|\xi\|_2 = 1} \inf_{\eta \in \mathcal{H}_2} \left\| \hat{H}_{f_1}^k \xi - \hat{H}_{f_2}^k \eta \right\|_2. \tag{57}$$

where $\xi, \eta \in \mathcal{H}_2, \|\xi\|_2 = 1$.

This expression can be interpreted as follows. For a given input unit ξ, we first search all η to identify the value that minimizes the difference in responses between the two systems (operation inf). Then, among all possible inputs ξ, we select the one that maximizes this minimal difference (operation sup).

Therefore, this quantity characterizes the maximum separable discrepancy between the two systems. In fact, there exists a pair (ξ, η) for which the norm $\|H_{f_1}^k \xi - H_{f_2}^k \eta\|_2$ can be made arbitrarily close to the K-gap distance δ_k. Consequently, this quantity characterizes the worst-case discrepancy between the two systems.

Thus,for some $\xi, \eta \in \mathcal{H}_2$ with $\|\xi\|_2 = 1$ and $\|\mathrm{R}\|_\infty = 1$.

$$\begin{aligned} &\delta_k\left(\mathcal{K}_K^{(f_1)}, \mathcal{K}_K^{(f_2)}\right) \\ &= \left\| \hat{H}_{f_1}^k \xi - \hat{H}_{f_2}^k \eta \right\|_2 \geq \left\| \mathrm{R}\left(\hat{H}_{f_1}^k \xi - \hat{H}_{f_2}^k \eta\right) \right\|_2 \end{aligned} \tag{58}$$

One can further obtain

$$\delta_k\left(\mathcal{K}_K^{(f_1)}, \mathcal{K}_K^{(f_2)}\right) \geq \left\| \mathrm{R}\, \hat{H}_{f_1}^k \xi \right\|_2 - \left\| \mathrm{R}\, \hat{H}_{f_2}^k \eta \right\|_2 \tag{59}$$

According to Equation (59), Equation (55) can also function as a fault isolation indicator by reflecting the disparity between $\left\|\hat{H}_{f_1}^k \xi\right\|_2$ and $\left\|\hat{H}_{f_2}^k \eta\right\|_2$. As demonstrated, the K-gap metric effectively distinguishes between residuals generated by the two fault models. More specifically, the terms $\begin{bmatrix} -\hat{N}_{f_1}^k & \hat{M}_{f_1}^k \end{bmatrix}$ and $\begin{bmatrix} -\hat{N}_{f_2}^k & \hat{M}_{f_2}^k \end{bmatrix}$ can be grouped together when the metric $\delta_k\left(\mathcal{K}_K^{(f_1)}, \mathcal{K}_K^{(f_2)}\right)$ is sufficiently small. Conversely, effective fault isolation becomes feasible when this metric is sufficiently large. Extending our previous work on gap metric-based fault detection, this study demonstrates that the K-Gap metric serves as a reliable fault isolation indicator. However, establishing appropriate thresholds is essential to ensure robust isolation performance, which leads to the following formal definition.

Definition 1. *The set of faults $\mathcal{K}_K^{(F_i)}$ is considered isolable if, for each $i = 1, 2, \ldots, L$, the following holds:*

$$\forall \mathcal{K}_K^{(F_i)} \in \mathcal{C}_{f_i},\ \mathcal{K}_K^{(F_j)} \notin \mathcal{C}_{f_j},\ i \neq j,\ j = 1, 2, \ldots, L$$

with each set $\mathcal{C}_{f_i}$ is defined as

$$\mathcal{C}_{f_i} \subseteq \left\{ \mathcal{K}_K^{(F_i)} : \delta_{K_{d,s}}^k\left(\mathcal{K}_K^{(f_i)}, \mathcal{K}_K^{(F_i)}\right) \leq \delta_i \right\},\ 0 < \delta_i < 1$$

where $\mathcal{K}_K^{(F_i)}$ denotes the SKR of a faulty system, while $\mathcal{C}_{f_i}$ refers to a fault cluster. As illustrated in Figure 1, this cluster has $\mathcal{K}_K^{(f_i)}$ as its center and δ_i as its radius.

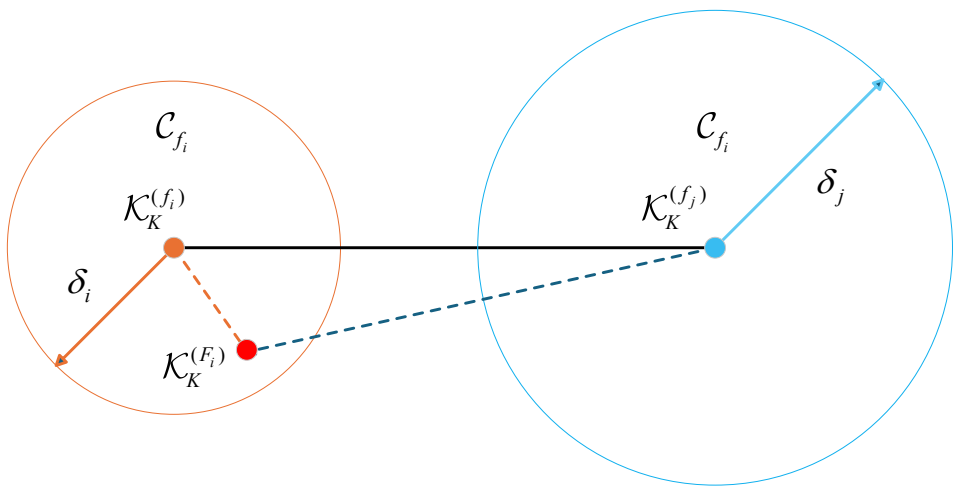

Figure 1. Schematic diagram of fault isolation based on the K-Gap metric.

Theorem 1. *Given the fault sets $\mathcal{K}_K^{(F_i)}$ and their corresponding clusters $\mathcal{C}_{f_i}$ with cluster centers $\mathcal{K}_{f_i}^k$ and radii δ_i for $i = 1, 2, \ldots, L$, the faults are isolable if*

$$\delta_{K_{d,s}}^k\left(\mathcal{K}_K^{(F_i)}, \mathcal{K}_K^{(F_j)}\right) > \delta_i + \delta_j, \quad \forall i \neq j, \quad i, j \in \{1, 2, \ldots, L\} \tag{60}$$

Proof. $\mathcal{K}_K^{(F_i)} \in \mathcal{C}_{f_i}$, $i \in \{1, \ldots, L\}$ and thus

$$\delta_{K_{d,s}}^k \left(\mathcal{K}_K^{(f_i)}, \mathcal{K}_K^{(F_i)} \right) \leq \delta_i \tag{61}$$

For any $j \in \{1, 2, \ldots, L\}$, $j \neq i$, the following inequality holds:

$$\delta_{K_{d,s}}^k \left(\mathcal{K}_K^{(f_i)}, \mathcal{K}_K^{(f_j)} \right) \leq \delta_{K_{d,s}}^k \left(\mathcal{K}_K^{(F_i)}, \mathcal{K}_K^{(f_i)} \right) + \delta_{K_{d,s}}^k \left(\mathcal{K}_K^{(F_i)}, \mathcal{K}_K^{(f_j)} \right)$$

This implies

$$\delta_{K_{d,s}}^k \left(\mathcal{K}_K^{(F_i)}, \mathcal{K}_K^{(f_j)} \right) \geq \delta_{K_{d,s}}^k \left(\mathcal{K}_K^{(f_i)}, \mathcal{K}_K^{(f_j)} \right) - \delta_{K_{d,s}}^k \left(\mathcal{K}_K^{(F_i)}, \mathcal{K}_K^{(f_i)} \right).$$

On the basis of Equation (59), one can obtain

$$\delta_{K_{d,s}}^k \left(\mathcal{K}_K^{(F_i)}, \mathcal{K}_K^{(f_j)} \right) > \delta_i + \delta_j - \delta_{K_{d,s}}^k \left(\mathcal{K}_K^{(F_i)}, \mathcal{K}_K^{(f_i)} \right) > \delta_j.$$

Consequently, $\mathcal{K}_K^{(F_i)} \notin \mathcal{C}_{f_j}$. According to Definition 1, the faults under consideration are therefore isolable. This proof is completed by noting that fault isolability is achieved if and only if there is no overlap among their corresponding clusters. □

Furthermore, the fault isolation scheme can be implemented with the following logic. If $\delta_{K_{d,s}}^k \left(\mathcal{K}_K^{(F_i)}, \mathcal{K}_K^{(f_i)} \right) \leq \delta_i$ and $\delta_{K_{d,s}}^k \left(\mathcal{K}_K^{(F_i)}, \mathcal{K}_K^{(f_j)} \right) > \delta_j$, then the fault satisfies $\mathcal{K}_K^{(F_i)} \in \mathcal{C}_{f_i}$; otherwise, $\mathcal{K}_K^{(F_i)} \notin \mathcal{C}_{f_i}$.

The fault isolation procedure given in Algorithm 3 for the data-driven K-Gap metric in nonlinear systems, represented by T-S fuzzy models follows a theoretical framework similar to the approach based on the Koopman operator. Therefore, its detailed derivation is omitted here.

Algorithm 3 Implementation of FDI

1. Input fault-free system data (u, y, x) and faulty system data (u^f, y^f, x^f);

2. Initialize the time period K, data-driven parameters s, N, and the number of recorded data points j;

3. Perform offline computation of the threshold J_{th}, δ_1, δ_2, and δ_3 based on Algorithm 1 ;

4. **For** $k = 1$ **to** K;

   4.1 **For** $z = 1$ **to** 3;

   4.1.1 Calculate J based on Algorithm 1;

   4.1.2 Calculate $\delta_{K_{d,s}}^K \left(\mathcal{K}_K^{(f)}, \mathcal{K}_K^{(f_z)} \right)$;

   4.2 **End For**;

Algorithm 3 *Cont.*

4.3 **If** $J > J_{\text{th}}$;

4.3.1 A fault is detected;

4.3.2 **If**
$\delta^K_{K_{d,s}}\left(\mathcal{K}^{(f)}_K, \mathcal{K}^{(f_1)}_K\right) < \delta_1$,
$\delta^K_{K_{d,s}}\left(\mathcal{K}^{(f)}_K, \mathcal{K}^{(f_2)}_K\right) > \delta_2$,
and
$\delta^K_{K_{d,s}}\left(\mathcal{K}^{(f)}_K, \mathcal{K}^{(f_3)}_K\right) > \delta_3$;

The fault is isolated in fault cluster $\mathcal{C}_{f_1}$;

4.3.3 **Else If**
$\delta^K_{K_{d,s}}\left(\mathcal{K}^{(f)}_K, \mathcal{K}^{(f_2)}_K\right) < \delta_2$,
$\delta^K_{K_{d,s}}\left(\mathcal{K}^{(f)}_K, \mathcal{K}^{(f_1)}_K\right) > \delta_1$,
and
$\delta^K_{K_{d,s}}\left(\mathcal{K}^{(f)}_K, \mathcal{K}^{(f_3)}_K\right) > \delta_3$;

The fault is isolated in fault cluster $\mathcal{C}_{f_2}$;

4.3.4 **Else If**
$\delta^K_{K_{d,s}}\left(\mathcal{K}^{(f)}_K, \mathcal{K}^{(f_3)}_K\right) < \delta_3$,
$\delta^K_{K_{d,s}}\left(\mathcal{K}^{(f)}_K, \mathcal{K}^{(f_1)}_K\right) > \delta_1$,
and
$\delta^K_{K_{d,s}}\left(\mathcal{K}^{(f)}_K, \mathcal{K}^{(f_2)}_K\right) > \delta_2$;

The fault is isolated in fault cluster $\mathcal{C}_{f_3}$;

4.3.5 **Else**;

The fault cannot be isolated;

4.3.6 **End If**;

4.4 **Else**;

Fault-free or undetectable;

4.5 **End If**;

5. **End For**;

6. **Return**
J, J_{th}, δ_1, δ_2, δ_3,
and
$\delta^K_{K_{d,s}}\left(\mathcal{K}^{(f)}_K, \mathcal{K}^{(f_z)}_K\right), \quad z = 1, 2, 3.$

6. Verifications

6.1. Simulation Environment and Parameters Setting

To validate the proposed FDI method, this study develops a SIMPACK-MATLAB/(SIMPACK 2018.1, MATLAB R2022b) Simulink co-simulation platform based on the structure of the CRH trailer and the monitoring points, as illustrated in Figure 2. The platform features a trailer model that incorporates active control forces, impossible faults, and track irregularities described by the Chinese high-speed low-excitation spectrum, thus realistically simulating the measurement of speed and vibration acceleration signals in the axle box and bogie.

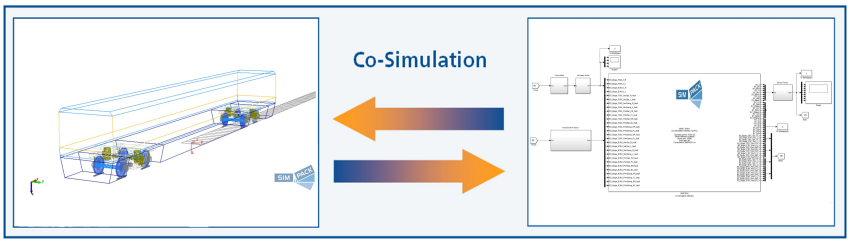

Figure 2. Co-simulaion platform.

In the aforementioned co-simulation environment, Simpack is used to construct a multi-body dynamics model to describe the suspension system, while Simulink is employed to design the fault detection and diagnosis architecture. The two platforms interact through a co-simulation interface. The simulation sampling frequency is set to 1000 Hz to ensure the stability and accuracy of the multi-body dynamics model, particularly under high-frequency vibration conditions of the suspension system. It is important to note that the 1000 Hz setting refers to the system simulation step size and does not imply that the fault diagnosis algorithm needs to operate at the same frequency. In practical applications, the sampling frequency for vibration signals is typically 1–5 kHz, whereas the diagnostic algorithm can run at a lower frequency (e.g., 100–200 Hz) or employ sliding windows and data downsampling strategies for processing. Furthermore, the method proposed in this paper primarily involves matrix operations and singular value decomposition. Given the computational capabilities of current onboard embedded processors (such as DSP or ARM platforms), and with a reasonable window length setting, the algorithm is entirely feasible for implementation.

The suspension system model incorporates nine nonlinear terms involving $\sin(\phi_0)$, $\sin(\theta_0), \ldots, \sin(\theta_2)$. Building on our previous work [24] on designing fuzzy rules for the suspension system, the T–S fuzzy rules adopted in this paper are formulated as follows:

$$
\begin{aligned}
&\textbf{Rule } \mathfrak{P}^1\text{:if } \phi(k) < -\alpha, \phi_1(k) < -\alpha \text{ and } \phi_2(k) < -\alpha,\\
&\text{then} \quad \delta^{T--S}_{K_{d,s}}(\mathcal{K}^{(o)}, \mathcal{K}^{(f)}) = \delta_{K_{1,d,s}}(\mathcal{K}^{(o)}_1, \mathcal{K}^{(f)})\\
&\textbf{Rule } \mathfrak{P}^2\text{:if } \phi(k) < -\alpha, \phi_1(k) < -\alpha \text{ and } \phi_2(k) \in [-\alpha, \alpha],\\
&\text{then} \quad \delta^{T--S}_{K_{d,s}}(\mathcal{K}^{(o)}, \mathcal{K}^{(f)}) = \delta_{K_{2,d,s}}(\mathcal{K}^{(o)}_2, \mathcal{K}^{(f)})\\
&\vdots\\
&\textbf{Rule } \mathfrak{P}^{27}\text{:if} \phi(k) > \alpha, \phi_1(k) > \alpha \text{ and } \phi_2(k) > \alpha,\\
&\text{then} \quad \delta^{T--S}_{K_{d,s}}(\mathcal{K}^{(o)}, \mathcal{K}^{(f)}) = \delta_{K_{27,d,s}}(\mathcal{K}^{(o)}_{27}, \mathcal{K}^{(f)})
\end{aligned}
$$

where the relevant parameters are consistent with those in [24] and are not reiterated here due to space constraints.

The computation of the Koopman operator via the Extended Dynamic Mode Decomposition (EDMD) algorithm typically relies on manually designed lifting functions. Based on the dynamic characteristics of the high-speed train suspension system, the selected lifting functions incorporate Fourier series, polynomial functions, and Gaussian kernel functions. Specifically, since the original nonlinear differential equations exhibit oscillatory and trigonometric terms due to vibration dynamics and coupling relationships, Fourier-series-based observables are introduced to capture the inherent periodic behaviors of the system. Polynomial and Gaussian kernel functions are further employed to characterize nonlinear coupling effects and local dynamic variations, respectively. The number of recorded data points is j = 30,000. In the simulation study, three types of multiplicative faults were considered, and the fault isolation radii achieved by different methods are presented in Table 1. The corresponding fault detection thresholds for the T-S fuzzy and Koopman-based methods are 0.204 and 0.235, respectively.

Table 1. Fault descriptions and isolation radius.

Fault Scenario	Case 1	Case 2	Case 3
Location	Secondary suspension actuator (air spring fault)	Primary suspension (spring fault)	Primary suspension (damper fault)
Time interval	$t \geq 20\,\mathrm{s}$	$t \geq 20\,\mathrm{s}$	$t \geq 20\,\mathrm{s}$
Performance degradation	−10%	−10%	−10%
Isolation radius δ_i (T–S fuzzy modeling)	0.00024	0.00031	0.00033
Isolation radius δ_i (Koopman modeling)	0.275	0.294	0.251

6.2. The Prediction of Suspension Dynamics Based on Koopman Operator

To ensure the feasibility of the FDI scheme, it is imperative to utilize the Koopman operator to accurately predict the dynamic characteristics of the train suspension systems under normal and various faulty conditions. Therefore, it is crucial to validate the effectiveness and robustness of the Koopman models constructed for the normal and fault modes. This validation involves comparing the model predictions with actual measurements to assess their prediction accuracy and generalization capability across different operational scenarios.

Figures 3 and 4 present the prediction results of the Koopman operator for the dynamic behavior of the high-speed train suspension system over 10,000 sampling points (equivalent to 10 s). These results cover both normal operation and a fault condition associated with the air spring in the secondary suspension actuator. Specifically, Figure 3 displays the predicted state variables (ϕ_0, ϕ_1, ϕ_2) under normal conditions, while Figure 4 shows the corresponding variables (z_0, z_1, z_2) for the system experiencing an air spring fault. The results indicate that the Koopman model effectively captures the system nonlinear dynamics, with the predicted trajectories showing strong agreement with the actual measurements. This finding validates the efficacy of the Koopman linearized model even in complex fault scenarios. To quantitatively evaluate the trajectory tracking accuracy, the Root Mean Square Error (RMSE) and Mean Absolute Error (MAE) are calculated for both scenarios. For Figure 3, the average RMSE and MAE are 3.003×10^{-5} and 1.896×10^{-5}, respectively. Meanwhile, the Figure 4 achieves an even lower average RMSE of 2.091×10^{-5} and an MAE of 1.077×10^{-5}. These micro-level errors demonstrate that the proposed model can reconstruct the latent state trajectories with exceptional precision.

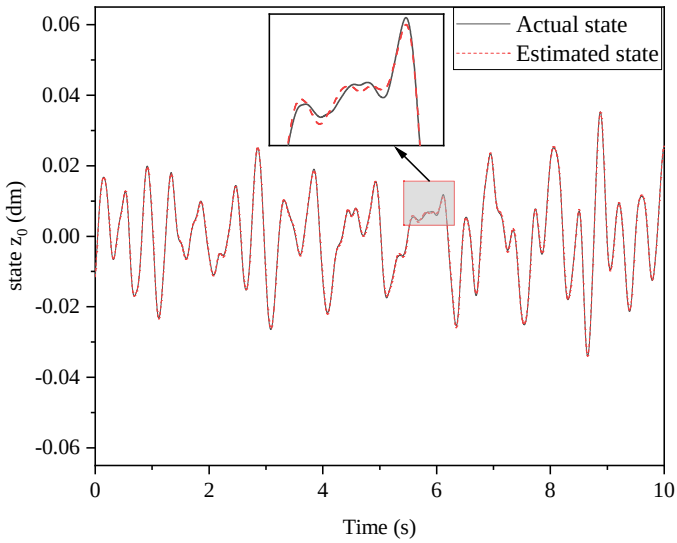

(**a**) Prediction result 1

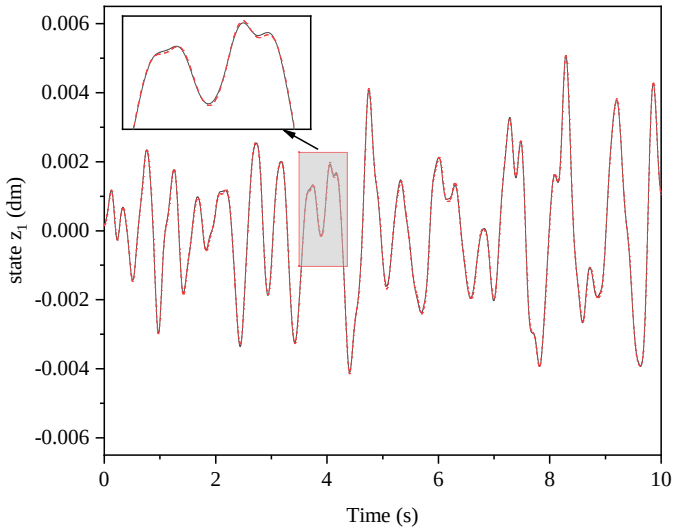

(**b**) Prediction result 2

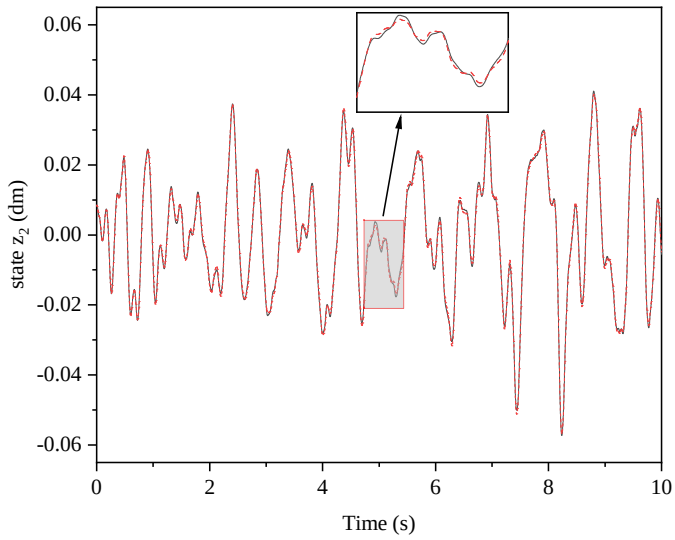

(**c**) Prediction result 3

Figure 3. Prediction of high-speed train suspension dynamics based on Koopman operator in fault-free case.

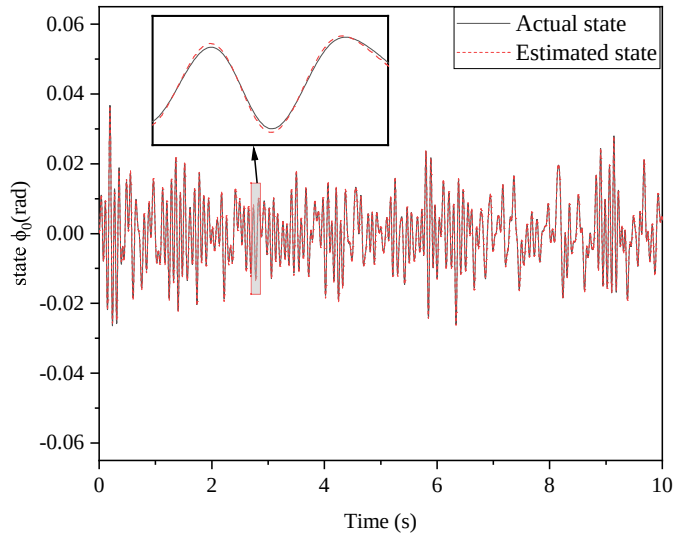

(**a**) Prediction result 1

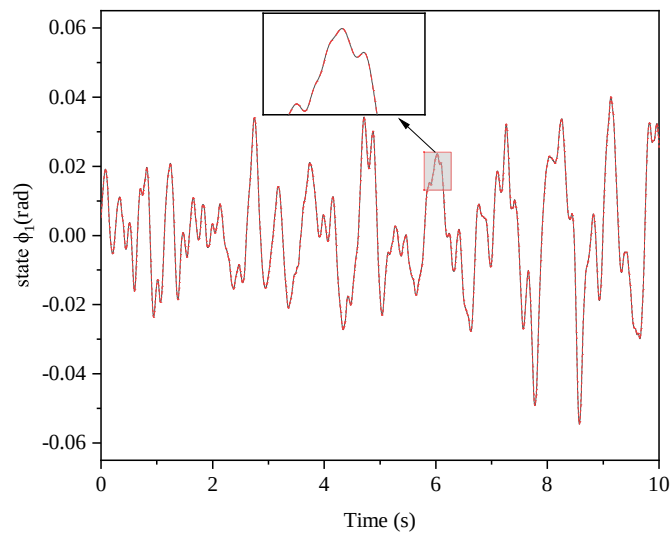

(**b**) Prediction result 2

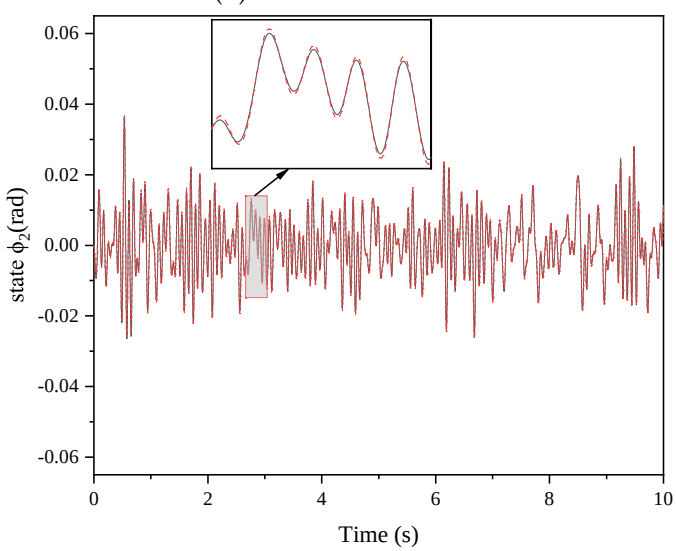

(**c**) Prediction result 3

Figure 4. Prediction of high-speed train suspension dynamics based on Koopman operator in faulty case.

6.3. Experimental Verification of FDI

Figures 5 and 6 compare the fault detection performance of T–S fuzzy models and Koopman-based approaches for three representative fault cases (Cases 1–3), where the data-driven K-Gap metric residuals are colored curves and the corresponding detection thresholds are red dashed lines. The Koopman-based K-Gap method demonstrates superior performance, exhibiting significantly greater variations in sensitivity between different types of faults compared to the T–S fuzzy approach. A limitation of the T–S model lies in its nearly indistinguishable K-Gap residual responses to faults that belong to the same suspension subsystem category. We attribute this limitation to the fact that manually configured fuzzy rules cannot sufficiently capture the nuanced data patterns of the suspension system. Although the T–S based K-Gap method is capable of fault detection, the poor distinguishability of its residuals poses challenges for subsequent fault isolation.

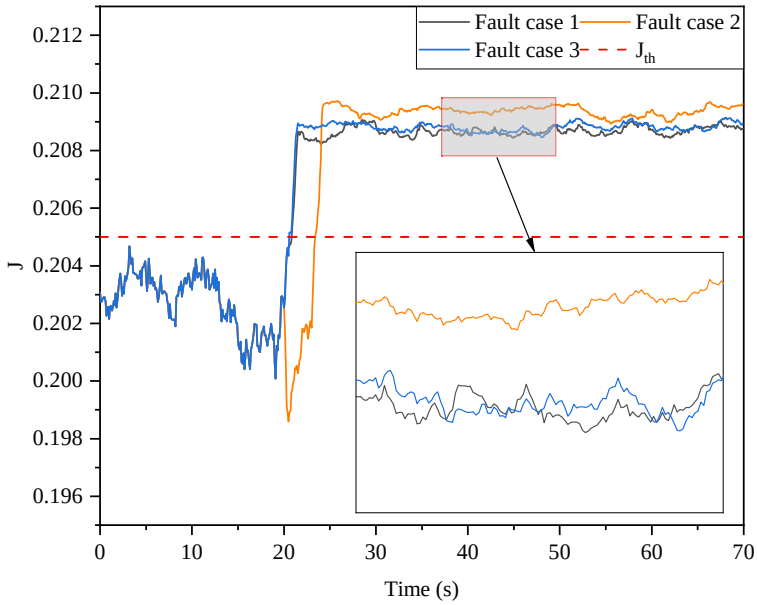

Figure 5. Fault detection results based on T–S fuzzy modeling [24].

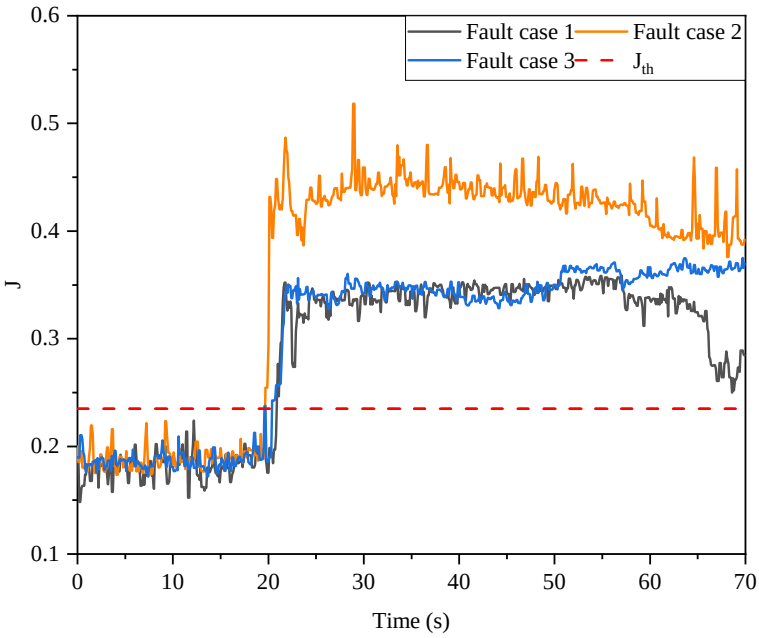

Figure 6. Fault detection results based on Koopman operator.

Figures 7 and 8 compare the fault isolation performance of the T–S fuzzy models and the Koopman-based methods for three representative fault scenarios (Cases 1–3). Correspondingly, the data-driven K-Gap metric residuals are depicted as colored curves, while the isolation boundaries are indicated by red dashed lines. Figure 7 specifically analyzes the faults that occur in the secondary suspension spring actuators using the T–S fuzzy approach. The results reveal that the post-fault K-Gap values become critically small and exhibit negligible variation, which fundamentally hinders reliable fault isolation. In contrast, Figure 8 shows that the globally linearized Koopman method generates sufficiently distinct K-Gap values, enabling clear differentiation between fault types. As presented in Tables 2 and 3, the Koopman operator-based method generally outperforms the T–S fuzzy modeling approach in terms of fault detection and isolation performance. Notably, it accomplishes fault isolation tasks that are unattainable with T–S fuzzy modeling. However, it should also be noted that due to the substantial computational overhead associated with data stacking in the Koopman operator, there may be observable latency issues in specific fault scenarios.

Table 2. Comparisons of fault detection rates.

	Fault Case 1	**Fault Case 2**	**Fault Case 3**
T–S fuzzy modeling	0.96	0.91	0.96
Koopman modeling	0.99	0.97	0.98

Table 3. Comparisons of Fault Isolation Rates.

	Fault Case 1	**Fault Case 2**	**Fault Case 3**
T–S fuzzy modeling	0	0	0
Koopman modeling	0.98	0.99	0.96
CNN	0.72	0.92	0.53
LSTM	0.56	0.95	0.36

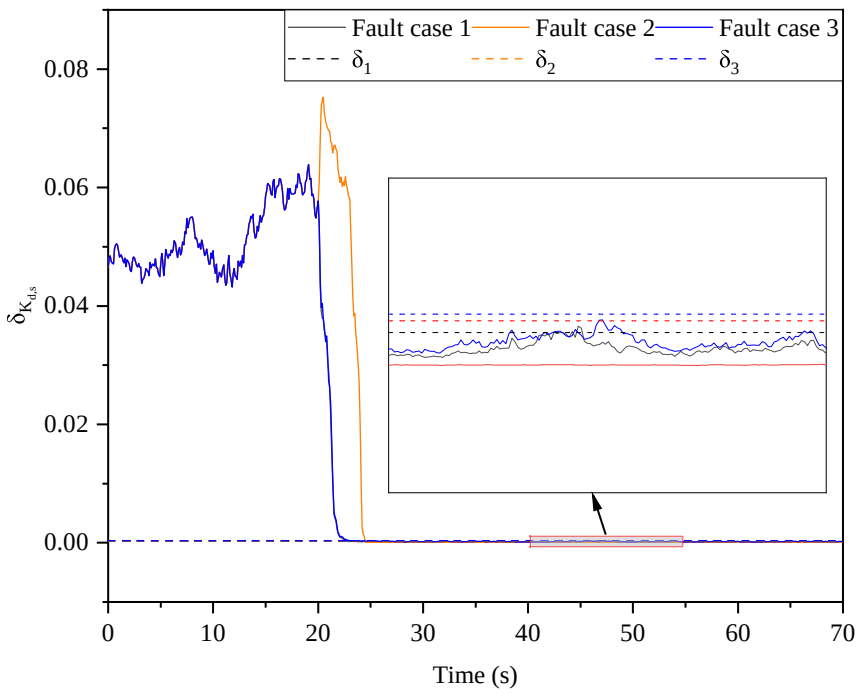

Figure 7. Fault isolation results based on T–S fuzzy modeling [24].

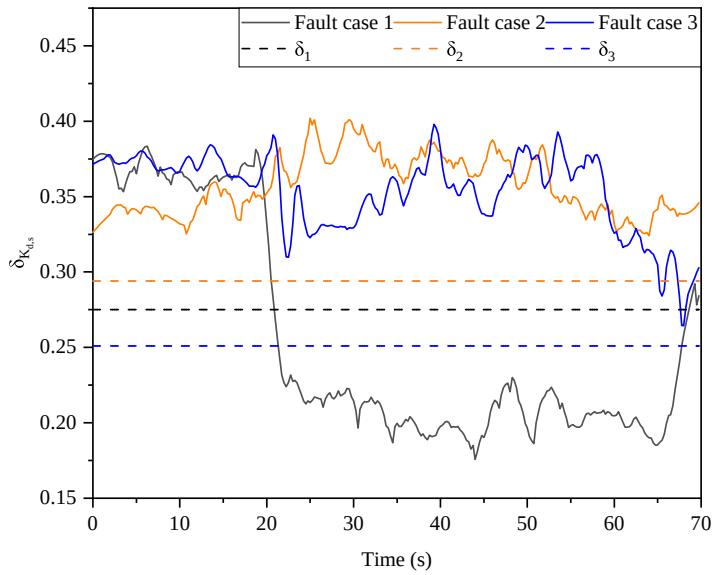

(**a**)

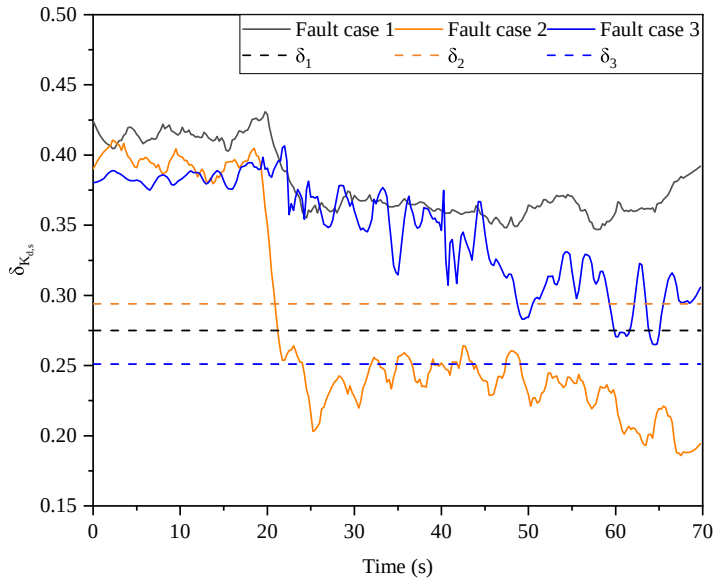

(**b**)

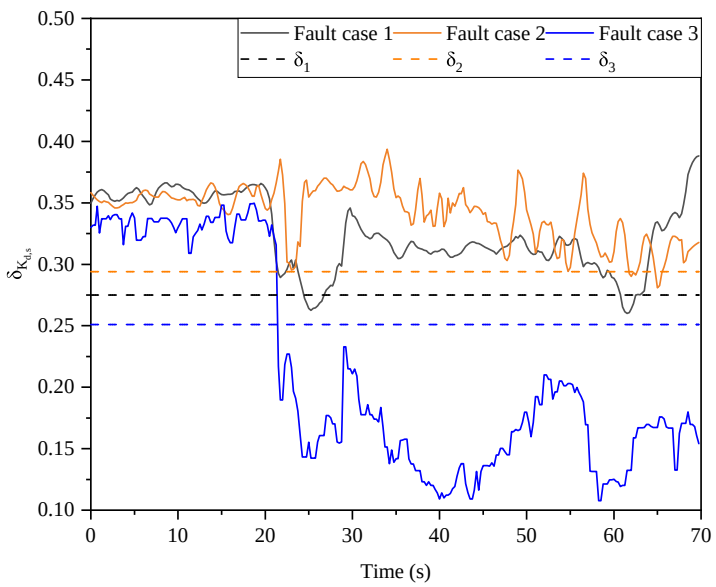

(**c**)

Figure 8. Fault isolation results based on Koopman operator: (**a**) Case 1; (**b**) Case 2; (**c**) Case 3.

In summary, the T–S fuzzy k-gap metric can achieve fault detection; however, it struggles to effectively accomplish fault isolation among different fault types. To further validate the effectiveness of the proposed Koopman k-gap metric in characterizing fault separability, comparative experiments with deep learning-based fault diagnosis methods were conducted. Specifically, CNN and LSTM, which are representative deep learning models for fault diagnosis, were selected as benchmark methods for comparison with the proposed approach . Among them, CNN can effectively extract local temporal features, while LSTM excels at modeling temporal dynamic dependencies. The fault isolation rates of different methods are presented in Table 3.

In the above comparative experiments, fault cases 1, 2, and 3 were assigned labels 1, 2, and 3, respectively. A sliding window with a length of 256 and a step size of 96 was used to generate samples from three types of fault data, and the dataset was divided into training and testing sets with a ratio of 8:2. All deep learning models were trained using the Adam optimizer with an initial learning rate of 1×10^{-3}. Specifically, the CNN model consisted of three convolutional layers, each followed by Batch Normalization, a ReLU activation function, and a pooling operation, in order to progressively extract local features from the fault signals. The LSTM model adopts a two-layer stacked architecture and achieves fault classification through recursive modeling of temporal information. The confusion matrices for fault isolation on the test set using the CNN and LSTM models are shown in Figures 9 and 10, respectively. The results show that both deep learning models perform well in identifying Fault case 2, but performance degrades for Fault case 1 and Fault case 3, with particularly evident misclassification for Fault case 3. Fault case 2 induces relatively significant system dynamic changes, producing distinguishable characteristic patterns that can be captured by both CNN and LSTM models. In contrast, the dynamic variations caused by Fault case 1 and Fault case 3 are relatively subtle, which increases the difficulty of fault classification. In particular, under Fault case 3, the system state deviation is small and the time varying characteristics are more pronounced. After sliding window segmentation, some samples contain insufficient fault information, making it difficult for the diagnostic model to learn stable and discriminative features, thereby resulting in a higher misclassification rate.

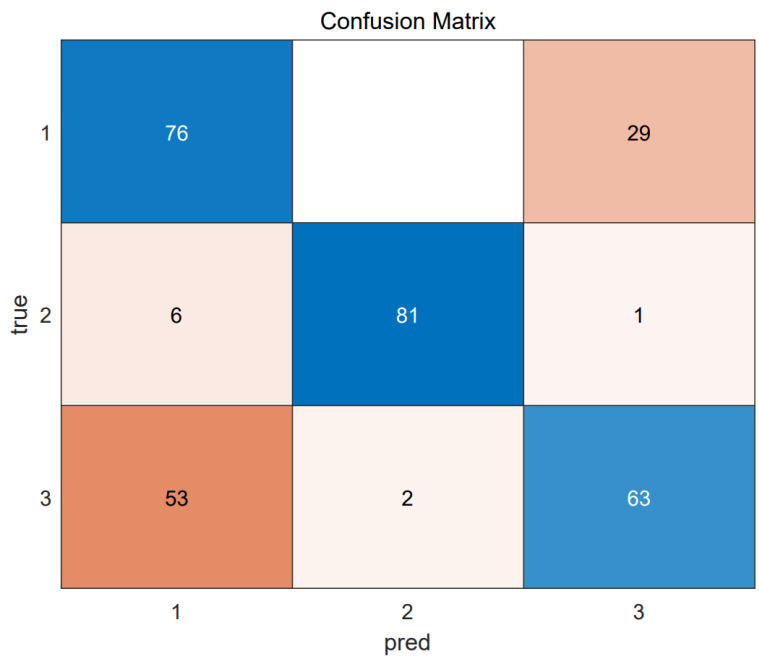

Figure 9. Fault isolation results based on CNN.

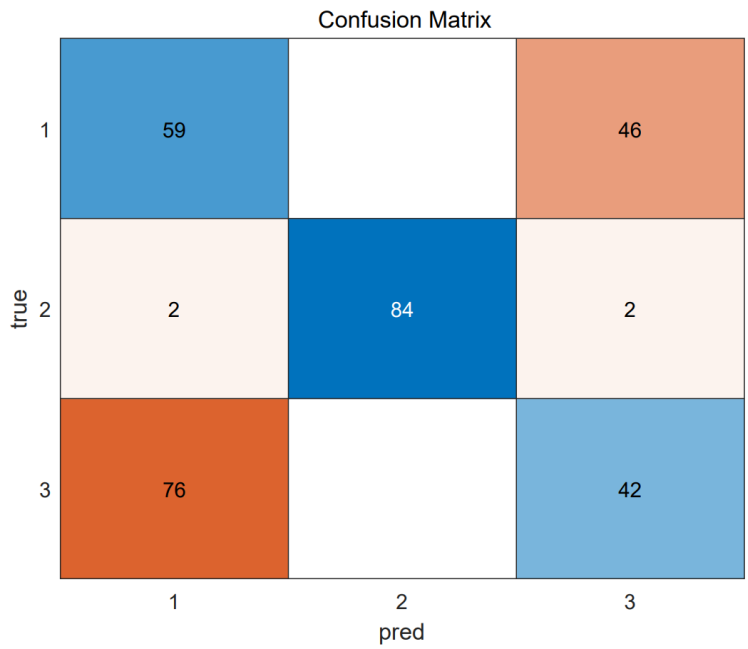

Figure 10. Fault isolation results based on LSTM.

The comparative scheme described above utilizes classification accuracy and confusion matrices to comprehensively evaluate the fault identification performance of different methods. Based on comprehensive experimental results, the proposed Koopman fuzzy k-gap method achieves the highest overall accuracy in fault isolation compared to deep learning methods such as CNN and LSTM. This conclusion can be attributed to the fundamental differences in the system modeling foundations between the Koopman fuzzy k-gap method and the other comparative schemes, and further validates its effectiveness in characterizing fault feature separability and achieving fault isolation performance. It should be particularly noted that the Koopman fuzzy k-gap method falls within the category of data-driven FDD schemes. However, the input/output representation of the system is derived from its analytical structure, implying that it contains more prior knowledge information about the system. In contrast, deep learning-based FDD methods mainly rely on process data and cannot fully utilize the prior knowledge embedded in physical models. Coupled with the limitations of available data, this further restricts their fault detection and isolation performance.

Experimental results demonstrate that the Koopman operator based K-Gap method surpasses the T–S fuzzy model in the task of identifying multiplicative faults in nonlinear systems. Although both approaches facilitate data-driven fault detection using the K-Gap metric, the T–S model suffers from two major limitations: (1) an inability to generate discriminative residual patterns across different fault categories, and (2) insufficient separation between fault clusters, leading to higher misclassification rates. These shortcomings originate from the dependence of the T–S model on manually designed fuzzy rules and its linearization framework, which limits its ability to fully capture the global dynamics of the system. Consequently, essential fault-related features are lost, often resulting in overlapping K-Gap residuals with minimal inter-class distances, a key factor that severely compromises fault isolation accuracy. In contrast, the Koopman operator based fault isolation method maps the system state space into a high-dimensional observable space, achieving a globally linear representation of the nonlinear system dynamics. This approach not only preserves the global dynamical information of the system, but also effectively captures subtle fault-induced deviations in the high-dimensional space. Consequently, within the Koopman framework, the K-Gap metric exhibits greater sensitivity to the dynamic characteristics

of different faults, substantially improving the accuracy of both fault detection and isolation. This advantage is particularly evident for slowly evolving or multiplicative faults. Benefiting from its global modeling capability, the Koopman method accurately reveals their cumulative effects and demonstrates significantly superior performance compared to the locally linearized T–S model. Thus, the Koopman operator offers a robust theoretical foundation and a distinct practical advantage for efficient and precise fault isolation in nonlinear systems.

7. Conclusions

This study leverages Koopman operator theory to develop a globally linearized computational framework for data-driven SKR in nonlinear systems. It extends the data-driven K-Gap metric fault diagnosis method to nonlinear domains, with a specific focus on addressing the challenging problem of detecting and isolating multiplicative faults in high-speed train suspension systems. Experimental results demonstrate that while both approaches achieve satisfactory fault detection performance, the Koopman operator based K-Gap metric exhibits a distinct superiority in fault isolation. This method can more effectively differentiate between various types of multiplicative fault residuals, preventing feature overlap in the residual space, and thereby improving isolation resolution. It is particularly well-suited for slowly evolving faults within closed-loop control architectures. In contrast, the T–S fuzzy approach suffers from limitations in complex nonlinear settings, including local modeling inadequacies, poor fault separability, and sensitivity to rule configuration, which constrain its robustness and practical applications.

Future research will focus on the integration of fuzzy neural networks and Koopman operator theory, with the aim of constructing an interpretable neural network architecture capable of adaptively learning optimal lifting functions. Simultaneously integrating the framework of graph theory and multi-agent systems [34,35] to improve the real-time performance and precision of fault diagnosis for structurally-complex nonlinear systems. This research will provide a new technical pathway for building intelligent diagnostic systems that balance interpretability with computational efficiency. Furthermore, in the process of designing the aforementioned diagnostic architecture, robustness under high-noise or severe uncertainty conditions, as well as generalization capabilities for various fault types (such as additive faults, sensor biases, or intermittent faults) will be a central focus of the research.

Author Contributions: All authors participated in the experiments and manuscript preparation. Y.W., Z.L. and Y.Z. contributed to the revision and polishing of the manuscript. All authors have read and agreed to the published version of the manuscript.

Funding: This work was supported in part by the National Natural Science Foundation of China under Grant No. 62573213, in part by the Fundamental Research Project of Zhenjiang (Grant No. JC2024014).

Data Availability Statement: Dataset available on request from the authors. The raw data supporting the conclusions of this article will be made available by the authors on request.

Conflicts of Interest: The authors declare no conflicts of interest.

References

1. Na, J.; Huang, Y.; Wu, X.; Su, S.-F.; Li, G. Adaptive finite-time fuzzy control of nonlinear active suspension systems with input delay. *IEEE Trans. Cybern.* **2020**, *50*, 2639–2650. [PubMed]
2. Li, M.; Shi, P.; Liu, M.; Zhang, Y.; Wang, S. Event-triggered-based adaptive sliding mode control for T–S fuzzy systems with actuator failures and signal quantization. *IEEE Trans. Fuzzy Syst.* **2021**, *29*, 1363–1374.

3. Ye, Y.; Li, H.; Li, F.; Gao, H.; Mei, G.; Dai, H.; Wu, P.; Zeng, J. Online assessment of train hunting stability by monitoring dynamic wheel–rail displacement: Why and how? *Nonlinear Dyn.* **2024**, *112*, 11993–12017. [CrossRef]
4. Hong, N.; Li, L.; Yao, W.; Zhao, Y.; Cai, Y.; Lin, J.; Tsui, K.L. High-speed rail suspension system health monitoring using multi-location vibration data. *IEEE Trans. Intell. Transp. Syst.* **2020**, *21*, 2943–2955. [CrossRef]
5. Yan, S.; Xia, Y.; Zhai, D.-H. Independent observers-based fault diagnosis for multiple sensor faults of full-vehicle active suspension systems with inaccurate models. *IEEE Trans. Autom. Sci. Eng.* **2025**, *22*, 12358–12370.
6. Han, S.-Y.; Zhou, J.; Chen, Y.-H.; Zhang, Y.-F.; Tang, G.-Y.; Wang, L. Active fault-tolerant control for discrete vehicle active suspension via reduced-order observer. *IEEE Trans. Syst. Man. Cybern. Syst.* **2021**, *51*, 6701–6711.
7. Liu, D.; Yang, Y.; Li, L.; Ding, S.X. Control performance-based fault-tolerant control strategy for singular systems. *IEEE Trans. Syst. Man. Cybern. Syst.* **2020**, *50*, 2398–2407. [CrossRef]
8. Wu, Y.; Su, Y.; Shi, P. Data-driven ToMHR-based incipient fault detection and estimation for high-speed rail vehicle suspension systems. *IEEE Trans. Ind. Inform.* **2025**, *21*, 613–622.
9. Cheng, C.; Qiao, X.; Luo, H.; Wang, G.; Teng, W.; Zhang, B. Data-driven incipient fault detection and diagnosis for the running gear in high-speed trains. *IEEE Trans. Veh. Technol.* **2020**, *69*, 9566–9576.
10. Chen, H.; Jiang, B.; Lu, N.; Mao, Z. Deep PCA based real-time incipient fault detection and diagnosis methodology for electrical drive in high-speed trains. *IEEE Trans. Veh. Technol.* **2018**, *67*, 4819–4830.
11. Liao, Y.; Geng, J.; Guo, L.; Geng, B.; Cui, K.; Li, R. Transfer learning rolling bearing fault diagnosis method based on deep domain adaptive network. *Int. J. Innov. Comput. Inf. Control* **2025**, *21*, 209–225.
12. Xu, J.; Tong, Q.; Zhu, R.; Du, S.; Zhao, J.; Jiang, X.; Wang, B. A diffusion-based data augmentation framework for few-shot fault diagnosis of intelligent high-speed train components. *Sensors* **2026**, *26*, 3091. [CrossRef] [PubMed]
13. Zhang, R.; Lee, S.-H.; Lee, K.-M.; Choi, Y.-S. Fault detection of high-speed train traction system based on probability-related slow feature analysis. *Energies* **2025**, *18*, 6073.
14. Ding, S.X. *Advanced Methods for Fault Diagnosis and Fault-Tolerant Control*; Springer: Berlin/Heidelberg, Germany, 2021.
15. Li, L.; Ding, S.X. Optimal detection schemes for multiplicative faults in uncertain systems with application to rolling mill processes. *IEEE Trans. Control Syst. Technol.* **2020**, *28*, 2432–2444. [CrossRef]
16. Wang, Y.; He, P.; Shi, P.; Zhang, H. Fault detection for systems with model uncertainty and disturbance via coprime factorization and gap metric. *IEEE Trans. Cybern.* **2022**, *52*, 7765–7775. [PubMed]
17. Ding, S.X. Application of factorization and gap metric techniques to fault detection and isolation part I: A factorization technique based FDI framework. *IFAC-PapersOnLine* **2015**, *48*, 113–118. [CrossRef]
18. Ding, S.X. Application of factorization and gap metric techniques to fault detection and isolation part II: Gap metric technique aided FDI performance analysis. *IFAC-PapersOnLine* **2015**, *48*, 119–124. [CrossRef]
19. Li, L.; Ding, S.X. Gap metric techniques and their application to fault detection performance analysis and fault isolation schemes. *Automatica* **2020**, *118*, 109029. [CrossRef]
20. Koenings, T.; Krueger, M.; Luo, H.; Ding, S.X. A data-driven computation method for the gap metric and the optimal stability margin. *IEEE Trans. Autom. Control* **2018**, *63*, 805–810. [CrossRef]
21. Jin, H.; Zuo, Z.; Wang, Y.; Cui, L.; Li, L. An integrated model-based and data-driven gap metric method for fault detection and isolation. *IEEE Trans. Cybern.* **2022**, *52*, 12687–12697. [CrossRef] [PubMed]
22. Jin, H.; Zuo, Z.; Wang, Y.; Cui, L.; Zhao, Z.; Li, L.; Gao, Z. Small fault diagnosis with gap metric. *IEEE Trans. Syst. Man. Cybern. Syst.* **2023**, *53*, 5715–5728. [CrossRef]
23. Ni, F.; Mu, S.; Kang, J.; Xu, J. Robust controller design for maglev suspension systems based on improved suspension force model. *IEEE Trans. Transp. Electrif.* **2021**, *7*, 1765–1779. [CrossRef]
24. Wu, Y.; Su, Y.; Wang, Y.-L.; Shi, P. T–S fuzzy data-driven ToMFIR with application to incipient fault detection and isolation for high-speed rail vehicle suspension systems. *IEEE Trans. Intell. Transp. Syst.* **2024**, *25*, 7921–7932.
25. Zeng, Y.; Wang, Z.; Wu, L.; Lam, H.-K. Finite-time fault detection for stochastic nonlinear networked control systems via interval type-2 T–S fuzzy framework. *Nonlinear Dyn.* **2025**, *113*, 16493–16510.
26. Korda, M.; Mezić, I. Linear predictors for nonlinear dynamical systems: Koopman operator meets model predictive control. *Automatica* **2018**, *93*, 149–160. [CrossRef]
27. Korda, M.; Mezić, I. Optimal construction of Koopman eigenfunctions for prediction and control. *IEEE Trans. Autom. Control* **2020**, *65*, 5114–5129. [CrossRef]
28. Parmar, N.; Refai, H.H.; Runolfsson, T. A survey on the methods and results of data-driven Koopman analysis in the visualization of dynamical systems. *IEEE Trans. Big Data* **2022**, *8*, 723–738. [CrossRef]
29. Bruder, D.; Fu, X.; Gillespie, R.B.; Remy, C.D.; Vasudevan, R. Data-driven control of soft robots using Koopman operator theory. *IEEE Trans. Robot.* **2021**, *37*, 948–961.
30. Xiao, Y.; Zhang, X.; Xu, X.; Liu, X.; Liu, J. Deep neural networks with Koopman operators for modeling and control of autonomous vehicles. *IEEE Trans. Intell. Veh.* **2023**, *8*, 135–146. [CrossRef]

31. Bakhtiaridoust, M.; Yadegar, M.; Meskin, N. Data-driven fault detection and isolation of nonlinear systems using deep learning for Koopman operator. *ISA Trans.* **2023**, *134*, 200–211.
32. Lee, J.D.; Im, S.; Kim, L.; Ahn, H.; Bang, H. Data-driven fault detection and isolation for multirotor system using Koopman operator. *J. Intell. Robot. Syst.* **2024**, *110*, 128. [CrossRef]
33. Vinnicombe, G. *Uncertainty and Feedback: H∞ Loop-Shaping and the ν-Gap Metric*; Imperial College Press: London, UK, 2001.
34. Xu, H.; Lu, K.; Wang, Y.-L.; Zhu, Q. Online distributed algorithms for mixed equilibrium problems in dynamic environments. *Automatica* **2026**, *185*, 112771. [CrossRef]
35. Laptawee, S.; Tani, H.; Mai, N.T.; Hashikura, K.; Kamal, M.A.S.; Murakami, I.; San-Um, W.; Yamada, K. A design method of fault tolerant control systems using fault estimator for multi-plant systems. *Int. J. Innov. Comput. Inf. Control* **2025**, *21*, 227–237.

Disclaimer/Publisher's Note: The statements, opinions and data contained in all publications are solely those of the individual author(s) and contributor(s) and not of MDPI and/or the editor(s). MDPI and/or the editor(s) disclaim responsibility for any injury to people or property resulting from any ideas, methods, instructions or products referred to in the content.